THE DEGENERATE AND NON-DEGENERATE DEEP QUENCH OBSTACLE PROBLEM: A NUMERICAL COMPARISON

Ľubomír Baňas

Department of Mathematics
and the Maxwell Institute for Mathematical Sciences
Heriot-Watt University
Edinburgh EH14 4AS, UK

Amy Novick-Cohen

Department of Mathematics
Technion-IIT
Haifa 32000, Israel

Robert Nürnberg

Department of Mathematics
Imperial College London
London SW7 2AZ, UK

Abstract. The deep quench obstacle problem

$$(\textbf{DQ}) \quad \begin{cases} \frac{\partial u}{\partial t} = \nabla \cdot M(u)\nabla w, \\ w + \varepsilon^2 \triangle u + u \in \partial\Gamma(u), \end{cases}$$

for $(x,t) \in \Omega \times (0,T)$, models phase separation at low temperatures. In (DQ), $\varepsilon > 0$, $\partial\Gamma(\cdot)$ is the sub-differential of the indicator function $I_{[-1,1]}(\cdot)$, and $u(x,t)$ should satisfy $\nu \cdot \nabla u = 0$ on the "free boundary" where $u = \pm 1$. We shall assume that u is sufficiently smooth to make these notions well-defined. The problem (DQ) corresponds to the zero temperature "deep quench" limit of the Cahn–Hilliard equation. We focus here on a degenerate variant of (DQ) in which $M(u) = 1 - u^2$, as well as on a constant mobility non-degenerate variant in which $M(u) = 1$. Although historically more emphasis has been placed on models with non-degenerate mobilities, degenerate mobilities capture some of the underlying physics more accurately. In the present paper, a careful numerical study is undertaken, utilizing a variety of benchmarks as well as new upper bounds for coarsening, in order to clarify evolutionary properties and to explore the differences in the two variant models.

1. **Background.** While the deep quench obstacle free boundary problem (DQ) was apparently first proposed by Oono and Puri [44] as a phenomenological model for

phase separation, it can also be obtained from the Cahn–Hilliard equation [21, 20],

$$\textbf{(CH)} \quad \begin{cases} u_t = \nabla \cdot M(u)\nabla w, & (x,t) \in \Omega_T := \Omega \times (0,T), \\ w = \frac{\Theta}{2}\{\ln(1+u) - \ln(1-u)\} - u - \varepsilon^2\triangle u, & (x,t) \in \Omega_T, \\ n \cdot \nabla u = n \cdot M(u)\nabla w = 0, & (x,t) \in \Omega_T \times (0,T), \end{cases}$$

in the zero temperature or "deep quench" limit, $\Theta \to 0$. In (CH), $u \in [-1,1]$ denotes the difference of two concentrations, $\Theta \geq 0$ denotes a scaled absolute temperature, the mobility $M(u)$ is nonnegative, $\varepsilon > 0$ is a gradient energy coefficient, Ω is a smooth bounded domain in $\mathbb{R}^d$, $d = 1, 2, 3$, n denotes the unit exterior normal to Ω, and $0 < T < \infty$ is a given positive time. Typically one assumes for (CH) that $M(u) = 1$ or $M(u) = 1 - u^2$, and the resultant equations shall be referred to here, respectively, as the non-degenerate and the degenerate Cahn–Hilliard equations. The derivation of both variants of (CH) can be found in a series of papers by Cahn and Hilliard [14, 12, 29]; see also [42]. For the sake of simplicity, most early studies considered (CH) with constant mobility, often replacing the logarithmic term by a polynomial approximation, see for example [22, 19, 21, 17, 7]. More recently, with the growing interest in higher order degenerate parabolic equations such as the thin film equation, numerous studies have also focused on the Cahn–Hilliard equation as it appears in (CH), with degenerate mobility; see for example [20, 8].

In terms of existence, the following results may be stated for (DQ) [10, 20].

Theorem 1.1. *Let $\varepsilon > 0$, and let Ω be a bounded domain in $\mathbb{R}^d$, $d = 1, 2, 3$, with either $\partial\Omega \in C^{1,1}$ or Ω being convex. Let $(\cdot, \cdot)$ denote the $L^2(\Omega)$ inner product, and let $\langle \cdot, \cdot \rangle$ denote the $H^1(\Omega), (H^1(\Omega))'$ duality pairing. Suppose moreover that $u_0 \in \mathcal{K} := \{\eta \in H^1(\Omega) : |\eta| \leq 1\}$. Then there exists a pair $\{u, w\}$, such that $u \in L^2(0, T; H^2(\Omega)) \cap H^1(0, T; (H^1(\Omega))') \cap L^\infty(0, T; \mathcal{K})$, $w \in L^2(\Omega_T)$, with $w \in H^1_{loc}(\{M(u) > 0\})$ for a.e. $t \in (0, T)$, and*

$$\begin{cases} \langle \frac{\partial u}{\partial t}, \eta \rangle + \int_{\{M(u)>0\}} \nabla w \cdot M(u)\nabla\eta \, \mathrm{d}x = 0, & \forall \eta \in H^1(\Omega), \quad a.e. \ \ t \in (0, T), \\ \varepsilon^2(\nabla u, \nabla\eta - \nabla u) - (u, \eta - u) \geq (w, \eta - u), & \forall \eta \in \mathcal{K}, \quad a.e. \ \ t \in (0, T), \\ u(x, 0) = u_0, \quad x \in \Omega. \end{cases}$$

$$(1)$$

Moreover, in the case of constant mobility, the solution $\{u, w\}$ is unique if $\overline{u}_0 \in (-1, 1)$, where $\overline{\eta} := \frac{1}{|\Omega|}(\eta, 1)$ for $\eta \in L^1(\Omega)$.

These results were first proven for $M(u) = 1$ by Blowey & Elliott [10], and later for $M(u) = 1 - u^2$ by Elliott & Garcke [20]. They may be demonstrated by considering appropriate limits of solutions to the degenerate and non-degenerate (CH) equation, respectively, [10, 21, 20]. We remark that weaker formulations, such as that considered in [8, 18], are conceivable. For later use we note that a solution $\{u, w\}$ to (1) satisfies

$$\overline{u}(t) = \overline{u}_0 \qquad \forall \ t \in (0, T).$$

If initial conditions are taken which correspond to a small perturbation of a constant state u_0, then the dynamics for the deep quench obstacle problem (DQ) and for the Cahn–Hilliard equation (CH) are roughly similar, both for non-degenerate and degenerate mobilities, if the initial conditions lie within the linearly unstable regime (the "spinodal"). For (DQ), as long as $u_0 \in (-1, 1)$, the initial conditions lie within the linearly unstable regime; for (CH) the condition is similar though somewhat more restrictive. The basic stages of evolution include an initial period of

linear instability which marks the onset of phase separation (spinodal decomposition or the linear regime), followed by an intermediate regime during which local **saturation** to "near equilibrium" phases occurs throughout most of the domain, and finally a **coarsening regime** during which the characteristic dimensions of the support of the equilibrium phases grow. The initial conditions prescribed above are physically reasonable and easily implemented, and the various qualitative stages in the evolution of the dynamics have often been reported experimentally, see e.g. [51].

Clearly, although the dynamics for all these various models are quite similar in some wide sense, the various models are not mathematically equivalent. Hence, to facilitate comparison with experiment and to refine our understanding of the underlying dynamic processes, it becomes desirable to characterize the differences. The purpose of the present paper is to study the properties of these models and to benchmark the differences. In mathematical terms, this entails analysis of various rates, time scales, and length scales, utilizing a variety of tools and qualitative descriptors to get a careful hold on the dynamics. We outline below some of these tools and descriptors, and their realm of applicability.

The linear regime: Linear instability and saturation. If $\overline{u}_0$ is taken to lie within the linearly unstable regime and u_0 is prescribed as a perturbation of a constant state, then the early dynamics is dominated by linear (exponential) growth of the unstable modes, with a characteristic spatial scale corresponding to the fastest growing mode, [12, 42]. **How long does the linear regime last?** Early studies tended to emphasis the importance of the linear regime, because numerics and experiment appeared to indicate the dominance of a characteristic length scale which seemingly corresponded to the fastest growing mode of linear theory [27, 17]. **How long does the fastest growing mode maintain its dominance?** It has often been noted that the characteristic length scale of the linear regime seems to remains dominant well beyond the period of linear growth; this phenomenon had been explained in the context of the Cahn–Hilliard equation with $M(u) = 1$ [40, 46], but it has yet to be explored and explained within the context, for example, of (DQ) or (CH) with $M(u) = 1 - u^2$. Thus, the duration of the period of linear growth and the duration of the period of dominance of the system by the fastest growing mode constitute important benchmarks. **When does saturation occur?** Clearly, by the time saturation has occurred, the linear regime is indeed over. Analytically, we may define saturation via

$$S(t) := \frac{|\{x \in \Omega : |u(x,t)| = 1\}|}{|\Omega|}, \tag{2}$$

and so $S(t)$ constitutes an additional important benchmark.

Scaling behavior. A way to benchmark dynamics is to try to isolate scaling behaviors marked by characteristic rate constants and coefficients. In the present context, the idea is to identify certain time dependent functionals which provide some indication of the underlying length scales of the system, and to try to demonstrate numerically, and possibly analytically, a t^α growth for some $\alpha > 0$. Conceivably, more general scaling behaviors may occur. The focus here can be on **early time behavior** where the length scales are initially dictated by the underlying instability, or it can be on **late time behavior** where the length scales reflect the coarsening process. At least numerically, it should be possible to follow the evolution of various length scales from early times on through late times, in order to try to capture various interim, transient and **crossover behaviors**, [26].

While a wide variety of functionals could be considered in this context, a few, which are described below, have come into common use, and thus may be considered as benchmarks for the phase separation process.

The structure function. The structure function, or correlation length, is defined here for $k \in \mathbb{R}$ as

$$\mathbf{S}(k,\, t) = \frac{1}{|\{\mathbf{k};\, ||\mathbf{k}| - k| < 1\}|} \sum_{||\mathbf{k}| - k| < 1} \mathbf{S}_2(\mathbf{k},\, t)$$

where $\mathbf{S}_2(\mathbf{k},\, t) := |\{u(x,t) - \overline{u}_0\}\hat{\ }|^2(\mathbf{k}, t)$ for $\mathbf{k} \in \mathbb{R}^2$, with "ˆ" denoting the discrete Fourier transform. Most of the studies involving time dependence of the structure function during phase separation have focused on (CH) with constant mobility, and related constant mobility models, such as the phase field equations with constant mobility, and as such are not directly relevant. Moreover, the majority of the predictions and conjectures which have been proposed in regard to the structure function have not been rigorously justified [23, 24, 33]. In theory, analysis of microstructure could be undertaken based on consideration of higher order moments or correlations as well [28].

The free energy of the system. For (DQ), the free energy

$$E(t) := \frac{1}{2\,|\Omega|} \int_\Omega [\varepsilon^2 |\nabla u|^2 + (1 - u^2)]\, \mathrm{d}x, \tag{3}$$

acts as a Lyapunov functional for the system. Observing that

$$E(t) \geq \frac{\varepsilon}{|\Omega|} \int_\Omega (1 - u^2)^{1/2} |\nabla u|\, \mathrm{d}x = \frac{\varepsilon}{|\Omega|} \int_{\Omega \backslash \Omega_{saturated}} (1 - u^2)^{1/2} |\nabla u|\, \mathrm{d}x,$$

and setting $\mathcal{L}_0 := \inf_{u \in \mathcal{W}} \operatorname{Per}_\Omega \{u = +1\}$ where $\mathcal{W} := \{u \in BV : u = \pm 1 \text{ a.e.}, \overline{u} = \overline{u}_0\}$, it follows easily by adapting the arguments in [48] that

$$\frac{\varepsilon}{|\Omega|} \int_{\Omega \backslash \Omega_{\text{saturated}}} (1 - u^2)^{1/2} |\nabla u|\, \mathrm{d}x \geq \frac{\varepsilon \pi}{2|\Omega|} \mathcal{L}_0 + o(\varepsilon), \tag{4}$$

where $\frac{\varepsilon \pi}{2|\Omega|} \mathcal{L}_0$ may be identified as the Γ-limit of $E(t)$. In (4), $\frac{\varepsilon \pi}{2}$ corresponds to the free energy of a transition between $u = \pm 1$ in a 1D system at equilibrium, which has a transition width given by $\varepsilon \pi$ [10]. If the system is well saturated, then one may expect $\Omega \backslash \Omega_{\text{saturated}}$ to be partitioned into $\mathcal{L}(t)$ length of strips, where $\mathcal{L}(t) \geq \mathcal{L}_0 + o(1)$, with width $\varepsilon \pi$ and with energy per unit length given by $e = \frac{1}{2} \varepsilon \pi$, and hence $E(t) \approx \frac{1}{2|\Omega|} |\Omega \backslash \Omega_{\text{saturated}}| \approx \frac{1}{2}(1 - S(t))$. In particular

$$G(t) := E(t) - \frac{1}{2}(1 - S(t)) \tag{5}$$

should constitute an additional benchmark for saturation.

From the discussion above, we see that at late times most of the energy of the system is located in the interfacial regions of the system, and

$$E(t) \approx \frac{\varepsilon}{|\Omega|} \int_\Omega (1 - u^2)^{1/2} |\nabla u|\, \mathrm{d}x \approx \frac{\varepsilon \pi}{2|\Omega|} \mathcal{L}(t).$$

Thus in particular $E(t)$, as well as $\frac{2}{\varepsilon \pi} E$, should scale roughly as length^{-1} and provide an indication of the length scales of the system. The ratio of E^{-1} to the dominant length scale in the system depends on the precise definition which is adopted for the dominant length scale and reflects also the *geometric structure* of the solution.

In [36], upper bounds on the length scale were obtained at sufficiently long times and for sufficiently small initial energies, based on $[\frac{1}{t}]^{\frac{1}{3+\alpha}} \|E\|_{L^{3+\alpha}(0,t)} =$

$\left[\frac{1}{t}\int_0^t E^{3+\alpha}(\tau)\,d\tau\right]^{\frac{1}{3+\alpha}}$, which in terms of the scaling employed in our formulation may be stated as:

Theorem 1.2. *If $E(0)$ is sufficiently small and t is sufficiently large, then there exists a constant C_α, where $\alpha = 0$ for the constant mobility Cahn–Hilliard equation with polynomial free energy and $\alpha = 1$ for the degenerate mobility deep quench obstacle problem, which is independent of the geometry of $\Omega \subset \mathbb{R}^d$, such that*

$$\|E\|_{L^{3+\alpha}(0,t)} \geq \frac{1}{C_\alpha}\left(\frac{t}{\varepsilon^2}\right)^{\frac{1}{3+\alpha}}.$$

Note that it is not surprising that the scaling predictions differ for the degenerate and non-degenerate mobilities, since at late times the dynamics for (CH) with constant mobility is approximated by the Mullins–Sekerka problem [45, 1, 15], whereas the dynamics for (CH) with the degenerate mobility near the deep quench limit is approximated by motion by surface diffusion [13]. The late time dynamics for (DQ) with degenerate mobility have also been shown to be approximated by motion by surface diffusion [13].

Kohn and Otto noted in [36] that at sufficiently late times boundary effects dominate the dynamics, and the coarsening rate will fall far short of the predicted upper bounds. They also pointed out that it is not realistic to obtain lower bounds for coarsening, since there exist geometric configurations which do not coarsen; nevertheless, it is reasonable to expect realizable predictions for coarsening rates for initial data which is *generic* in some appropriate sense. For this reason, in our numerical studies, we average our results over many independent simulations.

Various dual norms. Various norms, or semi-norms, such as

$$L(t) := \sup_\xi\Big\{\frac{1}{|\Omega|}\int_\Omega u\xi\,\mathrm{d}x : \int_\Omega \xi\,\mathrm{d}x = 0,\ \xi\ \text{periodic},\ \sup_x \varepsilon|\nabla\xi| \leq 1\Big\},$$

can be defined which scale as length. Various other dual norms which scale as length are clearly also possible to consider.

Upper bounds on the length scale based on $S(0,t;r,\varphi) := \|E^\varphi L^{(\varphi-1)}\|_{L^r(0,t)}$ have been obtained for various (CH) and (DQ) models, under suitable restrictions on r, φ [36, 43]. For the deep quench obstacle problem, the results in [43, 41] may be somewhat strengthened using scaling arguments (see Appendix) to yield the following theorem. Let

$$\overline{E} = \overline{L} = \frac{1}{2}(1 - \overline{u}^2).$$

Theorem 1.3. *Let $\alpha = 0$ for the case of constant mobility and $\alpha = 1$ for the case of degenerate mobility, and set $t^* := \sup\{\{0\} \cup \{t \in (0,\infty)|E(t) \geq \frac{1}{2}(1 - \overline{u}^2)\}\}$. Then for any φ, r satisfying $0 \leq \varphi \leq 1$, $r < 3 + \alpha$, $\varphi r > 1 + \alpha$, $(1 - \varphi)r < 2$, there exist constants C_α, which are independent of the geometry of $\Omega \subset \mathbb{R}^d$ but which may depend on r, φ, $\overline{u}_0$, such that for $t > t^*$, for the case of nondegenerate mobility,*

$$S^{-1}(0,t;r,\varphi) \leq \overline{E}^{-\varphi}\overline{L}^{(1-\varphi)}\Big(\frac{\overline{E}t}{\varepsilon^2\overline{L}^2}\Big)^{\frac{1}{3}}\Big[\vartheta_1 - \Big(\frac{L^3(0)\varepsilon^2}{\overline{EL}t}\Big)^{\frac{3-r}{3}}\Big]^{-1/r}, \qquad (6)$$

where $0 \leq \varphi \leq 1$, $(1 - \varphi)r < 2$, $r < 3$, $\varphi r > 1$, and for the case of degenerate mobility,

$$S^{-1}(0,t;r,\varphi) \leq \overline{E}^{-\varphi}\overline{L}^{(1-\varphi)}\Big(\frac{2\overline{E}^2 t}{\varepsilon^2\overline{L}^2}\Big)^{\frac{1}{4}}\Big[\vartheta_2 - \Big(\frac{L^4(0)\varepsilon^2}{2(\overline{EL})^{\frac{1}{2}}t}\Big)^{\frac{4-r}{4}}\Big]^{-1/r}, \qquad (7)$$

where $0 \leq \varphi \leq 1$, $(1 - \varphi)r < 2$, $r < 4$, $\varphi r > 2$, and $\vartheta_i = \vartheta_i(\varphi, r)$ for $i \in \{1, 2\}$.

By evaluating these upper bounds for large t in the limit when $\varphi \to 1$, $r \to 3 + \alpha$ where $\alpha = 0$ in the nondegenerate case and $\alpha = 1$ in the degenerate case (see Appendix), we get for the case of nondegenerate mobility that

$$\Big[\frac{1}{t} \int_0^t E^3 \, d\tau\Big]^{-\frac{1}{3}} \leq \frac{2^{\frac{4}{3}}}{(1 - \overline{u}_0^2)^{\frac{4}{3}}} \Big[\frac{t}{\varepsilon^2}\Big]^{\frac{1}{3}}, \tag{8}$$

and for the case of degenerate mobility

$$\Big[\frac{1}{t} \int_0^t E^4 \, d\tau\Big]^{-\frac{1}{4}} \leq \frac{2^{\frac{5}{4}}}{(1 - \overline{u}_0^2)} \Big[\frac{t}{\varepsilon^2}\Big]^{\frac{1}{4}}, \tag{9}$$

with a similar approximate bound being implied for $E^{-1}(t)$. Experimentally, while the $t^{1/3}$ growth law has frequently been reported especially at late times [24, 33], various other growth laws have also been noted [33, 31, 30]. In particular, the predictions for the special case in which $\overline{u}_0$ is close to -1 or 1 are known to be particularly deviant and delicate [24, 49]. In deriving (6)–(9), the scalings $E \to E/\overline{E}$, $L \to L/\overline{L}$, $t \to t/\overline{t}$ were used, where $\overline{t} = \varepsilon^2 \overline{L}^2 / \overline{E}$ for the case of constant mobility and $\overline{t} = \varepsilon^2 \overline{L}^2 / (2\overline{E}^2)$ for the case of degenerate mobility. These scalings can also be employed in examining the results of other benchmarks.

Topological descriptors. We refer here to certain topological descriptors of the dynamics which may be evaluated using the tools of computational algebraic topology. The descriptors which we shall be considering here are the zeroth and first Betti numbers. The zeroth Betti number, β_0, is an integer indicating the number of connected components in the system, and the first Betti number, β_1, is an integer that counts the number of tunnels (in 3D) or loops (in 2D). They may be evaluated by postprocessing numerical computations using public domain software called CHomP [34, 35].

As in [25], we set

$$X^+(t) := \{x \in \Omega : u(x, t) > \overline{u}_0\}, \quad X^-(t) := \{x \in \Omega : u(x, t) < \overline{u}_0\}. \tag{10}$$

It is then possible to define $\beta_{int,0}(X^+(t))$ to be the number of internal connected components of $X^+(t)$, and $\beta_{bdy,0}(X^+(t))$ to be the number of components of $X^+(t)$ which touch the boundary. Note that $\beta_{int,0}(X^+(t)) = \beta_1(X^-(t))$, and that $(|\Omega|/\beta_0(X^\pm(t)))^{1/2}$ define length scales for the system. Moreover, $\beta_{bdy,0}(X^+(t)) = \beta_0(X^+(t)) - \beta_1(X^-(t))$ corresponds to the *Euler characteristic*, which has been calculated using techniques from digital topology [37]. Note than when $\overline{u}_0 = 0$, $\beta_1(X^+(t)) = \beta_1(X^-(t))$ for an ensemble average, and hence in this case the Euler characteristic is given by $\beta_{bdy,0}(X^+(t)) = \beta_0(X^+(t)) - \beta_1(X^+(t))$. There exist additional topological quantifiers, such as the *matricity* and the *Minkowski functions*, which have been employed elsewhere [38, 39, 3, 28].

The approach followed in this paper, i.e. employing CHomP to compute the Betti numbers of the sets $X^\pm(t)$, was previously implemented in [25] in the context of the constant mobility Cahn–Hilliard equation with a polynomial free energy. From their calculations for (CH), it was possible to quantify boundary effects as a function of time and to give some indication of $\overline{u}_0$ and ε dependence. In particular, it was seen in [25] that early on in the evolution, $\beta_{int,0}(X^\pm(t)) \sim \beta_{bdy,0}(X^\pm(t))$ and during the later stages of the evolution, it appears that $\beta_{int,0}(X^\pm(t)) \ll \beta_{bdy,0}(X^\pm(t))$, and $\beta_0(X^\pm(t))$ could be used to show that a smooth transition from spinodal decomposition to nucleation and growth occurs as the "mean mass" $\overline{u}_0$ is varied. The dominant

phase becomes a single connected component as the mean mass, $\overline{u}_0$, is raised, and in parallel $\beta_1(X^\pm(t))$ increases and then subsides. As ε increases, there is enhanced monotonicity (decay) seen in $\beta_0(X^\pm(t))$, $\beta_1(X^\pm(t))$. In comparing stochastic and deterministic variants of the Cahn–Hilliard equation, more monotonicity is seen in the stochastic variants, with experiment [32] seeming to support the enhanced monotonicity.

We will employ a fully practical finite element approximation of (1), using linear finite elements in space and a backward Euler discretization in time. The interpretation of the numerical results focuses on the analysis and comparison of the dynamics, based on the various benchmarks described above.

The plan of the paper is as follows. Section 2 contains a description of the algorithm used in the computations, as well as an explanation of some of the specific considerations which guided us in undertaking the simulations. Some qualitative results are also given. In Section 3, results of the numerical simulations are presented for the Betti numbers, for $E^{-1}(t)$, for the saturation $S(t)$ and $G(t)$, and for the structure function. Section 4 summarizes the results of the numerics and provides some suggestions for further analysis and experiment. An Appendix follows, which contains a derivation of the upper bounds (6)–(8).

2. **Numerical simulations.** In our numerical simulations in this paper, we shall implement the following finite element approximation of (1), which was previously employed in [6] and is based on the approximation introduced in [8].

2.1. **The finite element approximation.** Let $\{\mathcal{T}^h\}_{h>0}$ be a family of partitions of Ω into disjoint open simplices σ with $h_\sigma := \operatorname{diam}(\sigma)$ and $h := \max_{\sigma \in \mathcal{T}^h} h_\sigma$, so that $\overline{\Omega} = \cup_{\sigma \in \mathcal{T}^h} \overline{\sigma}$. Associated with $\mathcal{T}^h$ is the finite element space

$$S^h := \{\chi \in C(\overline{\Omega}) : \chi\mid_\sigma \text{ is linear } \forall\, \sigma \in \mathcal{T}^h\} \subset H^1(\Omega).$$

We introduce also

$$K^h := \{\chi \in S^h : |\chi| \leq 1 \text{ in } \Omega\} \subset \mathcal{K} = \{\eta \in H^1(\Omega) : |\eta| \leq 1\}.$$

Let J be the set of nodes of $\mathcal{T}^h$ and $\{p_j\}_{j \in J}$ the coordinates of these nodes. Let $\{\chi_j\}_{j \in J}$ be the standard basis functions for S^h; that is $\chi_j \in S^h$ and $\chi_j(p_i) = \delta_{ij}$ for all $i, j \in J$. We introduce $\pi^h : C(\overline{\Omega}) \to S^h$, the interpolation operator, such that $(\pi^h \eta)(p_j) = \eta(p_j)$ for all $j \in J$. A discrete semi-inner product on $C(\overline{\Omega})$ is then defined by

$$(\eta_1, \eta_2)^h := \int_\Omega \pi^h(\eta_1(x)\,\eta_2(x))\,\mathrm{d}x.$$

Let $0 = t_0 < t_1 < \ldots < t_{N-1} < t_N = T$ be a partition of $[0, T]$ into possibly variable time steps $\tau_n := t_n - t_{n-1}$, $n = 1 \to N$. We set $\tau := \max_{n=1 \to N} \tau_n$, and consider the problem:

For $n \geq 1$, find $\{U^n, W^n\} \in K^h \times S^h$ such that

$$\left(\frac{U^n - U^{n-1}}{\tau_n}, \chi\right)^h + (\pi^h[M(U^{n-1})]\,\nabla W^n, \nabla \chi) = 0, \qquad \forall\, \chi \in S^h, \qquad (11\text{a})$$

$$\varepsilon^2\,(\nabla U^n, \nabla[\chi - U^n]) \geq (W^n + U^{n-1}, \chi - U^n)^h, \qquad \forall\, \chi \in K^h, \qquad (11\text{b})$$

where $U^0 \in K^h$ is an approximation of $u_0 \in \mathcal{K}$.

We will always use $U^0 \equiv \pi^h u_0$ for $u_0 \in C(\overline{\Omega})$.

For the nondegenerate mobility $M(u) \equiv 1$, convergence for (11a,b) was shown in [11] in space dimensions $d = 1, 2, 3$, and error bounds were derived. For the degenerate mobility $M(u) = 1 - u^2$, the numerical analysis for (DQ) is less straightforward. We recall that convergence for (11a,b) was shown in [8] in one space dimension, $d = 1$, using a weaker solution concept than that used in (1). In particular, the limiting solution there need not satisfy $u \in L^2(0, T; H^2(\Omega))$. An alternative numerical approximation for (DQ) was introduced in [9, 4], for which convergence to a solution satisfying (1) can be shown for $d = 1, 2, 3$. This method regularizes the degenerate mobility on the discrete level, in order to yield a discrete entropy bound. This makes this alternative algorithm less practical, and so we prefer to use (11a,b). Here we point out that the discrete free boundary of (11a,b) can advance at most one mesh point per time step. Hence in practice we will always choose the time step size τ sufficiently small, in order to avoid pathological cases such as the ones described in [8, p. 312].

In order to increase the efficiency of the implemented algorithm, we will use adaptive finite elements throughout. Here we make use of the finite element toolbox Alberta [47], and employ the mesh refinement strategy described in [9]. In particular, the interfacial regions will be resolved with at least 8 mesh points across the interface. Solving (11a,b) requires solving a nonlinear system of algebraic equations involving a variational inequality at each time step. Recently a robust multigrid solver for the solution of (11a) has been proposed in [5], and we employed this solver throughout our simulations.

2.2. **General considerations.** In the section which follows, we present results from various numerical experiments investigating the qualitative and quantitative behavior of solutions to (DQ) with degenerate and non-degenerate mobility, focusing primarily on the effects of varying ε and the mean mass, $\overline{u}_0$. Some points to note in regard to these calculations:

i) Since for $\Omega = (0, H)^2$, (DQ) may be rescaled by setting

$$x \to x/l,\, t \to t/l^2,\, \varepsilon \to \varepsilon/l,\, H \to H/l, \tag{12}$$

for any $l > 0$, this rescaling can be used to model larger systems by considering smaller values of ε. This rescaling has been utilized in Section 3.2 to verify the numerical algorithm by comparing the numerical results for different values of ε. In the calculations, unless otherwise stated, the system size was taken as $(0, 1)^2$ by setting $H = 1$ for any ε, and the end time, T, was taken as $T = \varepsilon^2 T^*$, where $T^* = 160$. The scaling (12) with $l = \varepsilon^*$ then implies that the results are equivalent to taking (1) with $\Omega = (0, (\varepsilon^*)^{-1})^2$, $\varepsilon = 1$, with rescaled time $t \in (0, T^*/(\varepsilon^*)^2)$.

ii) In each numerical experiment, we chose random initial data u_0 with mean $\overline{u}_0 = \overline{\overline{u}}_0$, where $\overline{\overline{u}}_0 \in (-1, 1)$ is a fixed given parameter. More specifically, after defining the random value $\widetilde{u}_0(p_j) = \overline{\overline{u}}_0 + \theta \mathcal{U}_j(-1, 1)$ at all mesh nodes $\{p_j\}_{j \in J}$, where $\mathcal{U}_j(-1, 1)$ are independent random variables with uniform distribution from the interval $(-1, 1)$ and θ denotes the amplitude of the random perturbation, we then set $u_0 = \widetilde{u}_0 + (\overline{\overline{u}}_0 - \overline{\widetilde{u}}_0)$. While we shall check the effects of varying θ, we have set $\theta = 0.05$ if not otherwise indicated.

iii) For the sake of comparison and simplicity, the time scale corresponding to $\varepsilon = 1$ has been indicated in all of the figures so that the dimensionless final time is 160, unless otherwise specified. To gain some intuition into this final time, note that in the context of (DQ), the (linear) growth rate of the fastest growing mode $\vec{k}_{fastest}$ is prescribed by $\sigma_{fastest} := \sigma(\vec{k}_{fastest}) = \frac{M(\overline{u}_0)}{4\varepsilon^2}$, see Section 3.4. In particular when
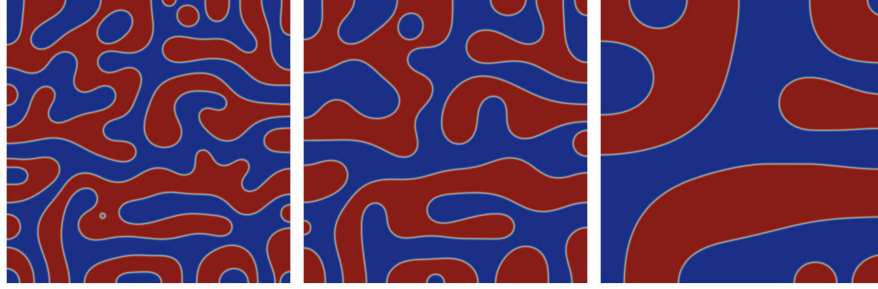
FIGURE 1. Contour plots of $u(t)$ at times $t = 80, 160, 1600$ for $M(u) = 1$. Here $\overline{u}_0 = 0$.
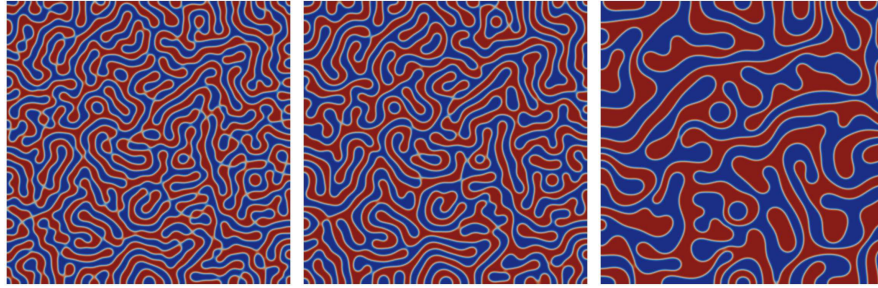

FIGURE 2. Contour plots of $u(t)$ at times $t = 80, 160, 1600$ for $M(u) = 1 - u^2$. Here $\overline{u}_0 = 0$.

$\overline{u}_0 = 0$, $M(\overline{u}_0) = 1$ for both constant and degenerate mobilities, and hence in both cases $\sigma_{fastest} = \frac{1}{4}$ when $\overline{u}_0 = 0$ and $\varepsilon = 1$. If we may roughly approximate the end of the linear regime t_{linear} when $\overline{u}_0 = 0$ by setting

$$||u(x, t_{linear})||_\infty \approx 1 \approx \theta e^{\sigma_{fastest} t_{linear}},$$

it then follows that $t_{linear} = -4 \ln(0.05) \approx 11.9828$, when $\theta = 0.05$, $\varepsilon = 1$, $\overline{u}_0 = 0$. Thus in the context of this choice of parameters, $t_{final} \approx 13.6361 \, t_{linear}$.

In all of the following plots, in order to reduce the effect of noise, we report on the averaged quantities over a certain number of N independent simulations, usually $N = 50$. Similar procedures have been adopted numerous times in the past, see e.g. [50], to attain some degree of genericity in the numerical results [36, 40, 46]; our results will nevertheless be influenced by boundary effects which can only be reduced by considering larger systems, or mimicked to some degree by considering smaller values of ε.

3. Results.

3.1. **Qualitative results.** The qualitative evolution from random initial data can clearly be seen in Figures 1 and 2. As mentioned in the introduction, phase separation starts with spinodal decomposition, followed by a saturation phase, and finally by a coarsening phase. Figure 1 portrays the evolution from random initial data for constant mobility $M(u) = 1$, while the evolution from the same random initial data for the degenerate case $M(u) = 1 - u^2$ is shown in Figure 2. In both cases we set $\overline{u}_0 = 0$. One can clearly see that the constant mobility case $M(u) = 1$

leads to larger connected components, while the degenerate case retains many more fine details. This is clearly due in part to the effective decrease in the degenerate mobility as saturation is approached.

We performed several experiments where we observed the evolution of the free energy, $E(t)$, and the saturation, $S(t)$, defined respectively in (3) and (2), as well as the Betti numbers. Note that at fixed times t, $E(t)$, $S(t)$, as well as $G(t)$ which was defined in (5), are invariant under the rescaling (12). Later, the evolution of additional quantities such as $\mathbf{S}(k, t)$ will be observed. We varied the gradient energy coefficient ε as well as the mean initial mass, $\overline{u}_0 \in (-1, 1)$. To eliminate possible effects of numerical errors on the results, we computed the saturation approximately as:

$$S(t_n) := \frac{|\{x \in \Omega : |\,\|U^n(x)\| - 1| < tol_S\}|}{|\Omega|},$$

with $tol_S = 10^{-8}$. See Figure 3 where plots of $E^{-1}(t)$ and $S(t)$ for $\varepsilon = \frac{1}{64\pi}, \frac{1}{32\pi}, \frac{1}{16\pi}$ and $\overline{u}_0 = 0$ are portrayed. Note that here we take ε^{-1} to be multiples of π, so that the number of mesh points in our discretization from §2.1 across the asymptotic transition layer width of $\varepsilon\,\pi$ can be easily estimated. The evolution of both $E^{-1}(t)$ and $S(t)$ can be seen to be marked by three regimes: an initial period with little change in $E^{-1}(t)$ and $S(t)$, a transitional period during which the saturation increases steeply, as does the length scale to a lesser degree, and an extended period of continued coarsening and saturation. During the initial and transitional periods, the behavior is relatively similar for the constant and degenerate mobilities, whereas during the third period the growth in $E^{-1}(t)$ and $S(t)$ is considerably slower for the degenerate mobility. Both $E^{-1}(t)$ and $S(t)$ can be seen to exhibit scale invariance. Comments regarding the Betti numbers will be given in the next section.

3.2. **Calculation of the Betti numbers.** In this section we use the subroutines of CHomP [34, 35] to calculate the Betti numbers, β_0 and β_1, which measure respectively, the number of connected components and the number of tunnels or links. We shall denote by $\beta_0^\pm$ ($\beta_1^\pm$) the number of connected components (tunnels) of the set $X^\pm(t)$ defined in (10). Furthermore, we shall denote the number of internal components (i.e. the components that do not touch the boundary) of $X^\pm(t)$ by $\beta_{int,0}^\pm$ and the number of components of $X^\pm(t)$ touching the boundary by $\beta_{bdy,0}^\pm$. These quantities are evaluated based on CHomP calculations of $\beta_0^\pm$ and $\beta_1^\pm$, by making use of the relationships noted earlier which imply that $\beta_{int,0}^\pm = \beta_1^\mp$ and $\beta_{bdy,0}^\pm = \beta_0^\pm - \beta_{int,0}^\pm = \beta_0^\pm - \beta_1^\mp$.

The evolution of the various Betti numbers for $\overline{u}_0 = 0$ for $\varepsilon = \frac{1}{64\pi}$ is displayed in Figure 4. Not surprisingly, the evolution of the Betti numbers for the sets X^+ and X^- is almost identical when $\overline{u}_0 = 0$. Again, for the constant and degenerate mobilities, the behavior is similar during the initial and transitional periods, with slower growth (less decrease in the Betti numbers) during the third regime when the mobility is degenerate. The transition between the first and second regimes is seen to be smooth in the context of the evolution of the Betti numbers, with nonmonotonicity setting in for both mobilities before what appears to be the end of the first regime in the context of the evolution of $E^{-1}(t)$ and $S(t)$. Indeed, there is an actual increase in the number of connected components and tunnels, for a short period of time for both mobilities.

In Figure 5, for the case of constant mobility, the various Betti numbers have been portrayed for both $\varepsilon = \frac{1}{16\pi}$ and $\varepsilon = \frac{1}{32\pi}$ with $H = 1$, $H = 0.5$, respectively,
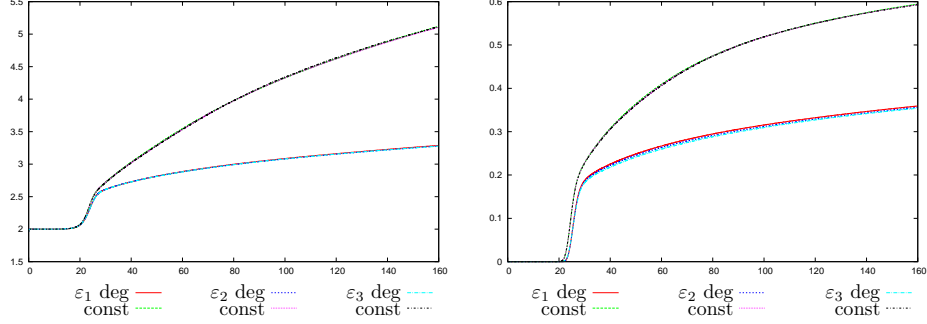
FIGURE 3. $E^{-1}(t)$ (left) and $S(t)$ (right) as functions of time, for $\varepsilon = \{\varepsilon_1, \varepsilon_2, \varepsilon_3\} = \{\frac{1}{64\pi}, \frac{1}{32\pi}, \frac{1}{16\pi}\}$, $\overline{u}_0 = 0$ with degenerate mobility (deg) and constant (const) mobility.
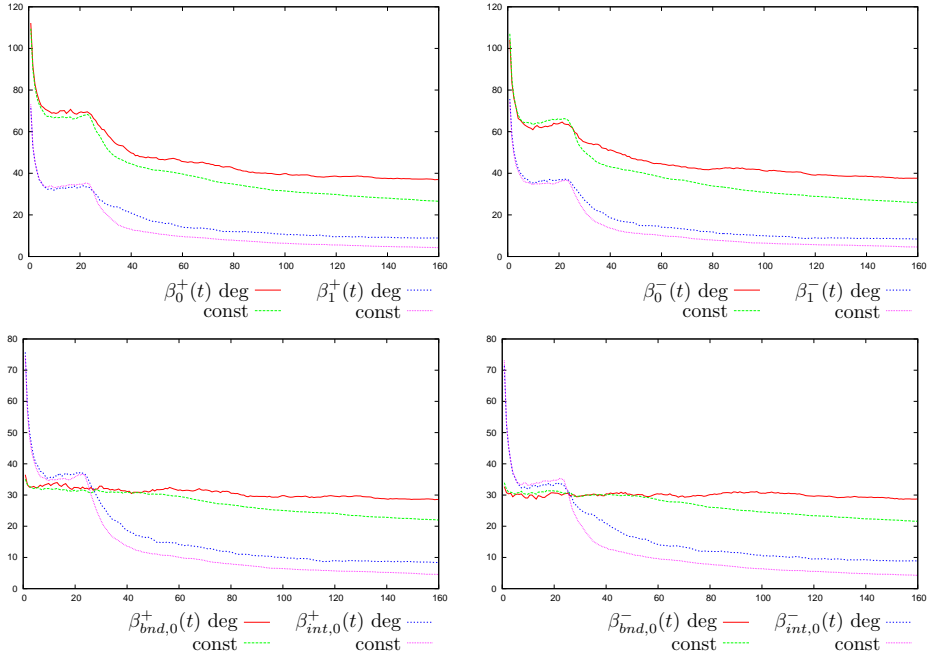

FIGURE 4. $\beta_0^\pm(t)$, $\beta_1^\pm(t)$, $\beta_{int,0}^\pm(t)$, $\beta_{bdy,0}^\pm(t)$ as functions of time, for $\varepsilon = \frac{1}{64\pi}$, $\overline{u}_0 = 0$.

with x and t rescaled in accordance with (12). The time scale in both these plots refers to the time scale for $\varepsilon = 1$. The results for both values of the ε parameter can be seen to be very similar in both figures. The results are in agreement with the scaling law (12). The minor differences can be attributed to the finite size of the system and the influence of the boundaries, as well as to sensitivity of the integer valued calculations. In [25] enhanced decay was seen with increasing ε, but a scaled comparison was not specifically undertaken there.
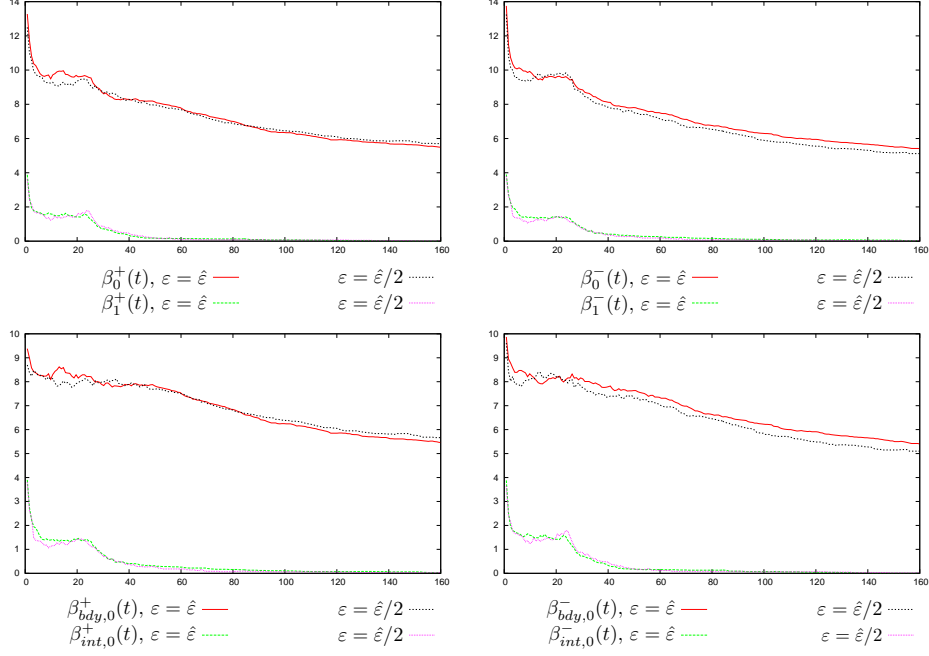
FIGURE 5. $\beta_0^\pm(t)$, $\beta_1^\pm(t)$, $\beta_{int,0}^\pm(t)$, $\beta_{bdy,0}^\pm(t)$ as functions of time, for $\varepsilon = \hat{\varepsilon} := \frac{1}{16\pi}$ ($H = 1$) and $\varepsilon = \frac{\hat{\varepsilon}}{2}$ ($H = 0.5$). Here we take $M(u) = 1$ and $\overline{u}_0 = 0$.
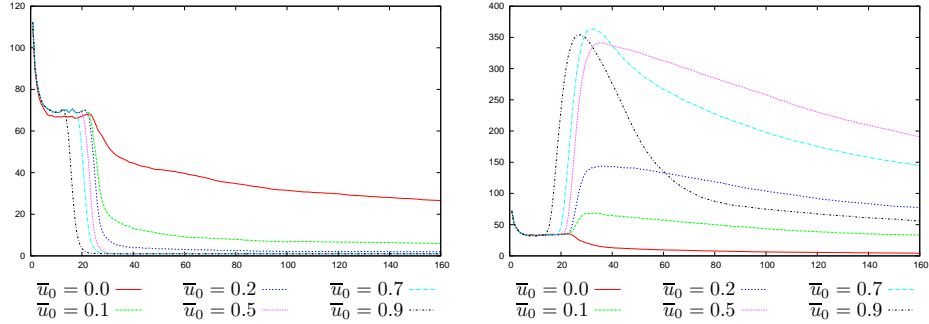

FIGURE 6. $\beta_0^+(t)$ (left) and β_1^+ (right), for $\varepsilon = \frac{1}{64\pi}$, and constant mobility.

The evolution of the Betti numbers was evaluated in simulations with $\overline{u}_0 = \{0, 0.1, 0.2, 0.5, 0.7, 0.9\}$ for $\varepsilon = \frac{1}{64\pi}$. To facilitate comparison, Figures 6, 7 contain 2D plots of the Betti numbers for the various values of $\overline{u}_0$. Looking at Figures 6 and 7, we can see that $\beta_0^+(t)$ seems for the most part to exhibit monotone decrease with time. For the constant mobility case, this decrease appears to be more pronounced as $\overline{u}_0$ increases. For the degenerate mobility case, this tendency occurs for $0 < \overline{u}_0 \leq 0.2$, and then reverses direction temporarily, apparently due to reduced mobility effects. During the initial stages, the evolution of $\beta_0^+(t)$ appears quite similar for
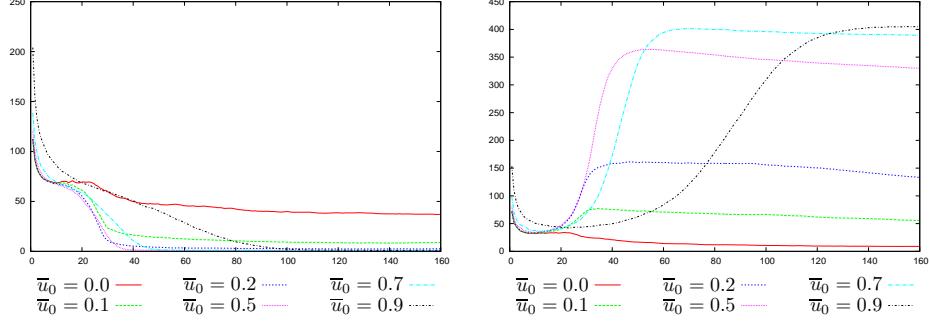
FIGURE 7. $\beta_0^+(t)$ (left) and β_1^+ (right), for $\varepsilon = \frac{1}{64\pi}$, and degenerate mobility.

the constant and degenerate mobilities and the various initial masses, $\overline{u}_0$, but as saturation is approached, the differences become more pronounced.

In [25] nonmonotonicity of $\beta_0^+(t)$ was reported, and that tendency can be seen here also, in Figures 6 and 7. The nonmonotonicity apparently reflects a reorganizational stage of sorts, while monotonicity only was reported in [25] when space-time noise was added to the model. For the case of constant mobility, the nonmonotonicity is enhanced with increasing $\overline{u}_0$, but at later times the effect is inverted. At long times, it is reasonable to expect there to be less loops when the mass fraction of the minor phase is small. For the degenerate mobility case, similar nonmonotonicity tendencies can be seen when $\overline{u}_0$ is not too large, with secondary effects occurring when $\overline{u}_0$ is larger due perhaps to reduced mobility effects. Again, during the initial stages, the evolution of $\beta_1^+(t)$ seems for the most part to be quite similar for both mobilities and for the different masses, with differences becoming more pronounced afterwards. We point out that any secondary transition phenomena cannot be linked with a possible transition from spinodal decomposition to nucleation behavior, since in the context of the deep quench obstacle problem, the "homogeneous free energy" $\phi(u) = 1 - u^2$ is uniformly concave, and hence the "binodal" and the "spinodal" coalesce and no metastable behavior is predicted [42].

In order to gain some intuition into boundary effects, $\beta_{int,0}^+/\beta_0^+$ has been plotted as a function of time in Figure 13, below. Initially $\beta_{int,0}^+$ is considerably larger than $\beta_{bdy,0}^+$ ($\beta_{int,0}^+/\beta_0^+ > \frac{1}{2}$) reflecting linear regime dynamics, and then there is an interim during which $\beta_{int,0}^+ \approx \beta_{bdy,0}^+$ ($\beta_{int,0}^+/\beta_0^+ \approx \frac{1}{2}$). During these early stages, the evolution is quite similar for both mobilities and for the various initial masses, $\overline{u}_0$, except for $\overline{u}_0 \approx 0.9$ in the degenerate case. Afterwards, $\beta_{int,0}^+ \ll \beta_{bdy,0}^+$ ($\beta_{int,0}^+/\beta_0^+ \ll \frac{1}{2}$), indicating a dominance of boundary components. This regime takes longer to be realized in the degenerate context, and at similar times $\beta_{int,0}^+/\beta_0^+$ can be seen to be smaller in the constant mobility case. The predominance of boundary components at late times can be explained in terms of lower dimensionality, which makes coarsening more difficult near the boundary. This phenomenon has been discussed by Alikakos et al. [2] within the Cahn–Hilliard framework in terms of the migration of minor phase "bubbles" toward the boundary of the domain. Such arguments seem to pertain better to the more diffusive constant mobility setting. In the degenerate setting, the internal components persist longer, due apparently to reduced communication between the components and less rapid motion towards
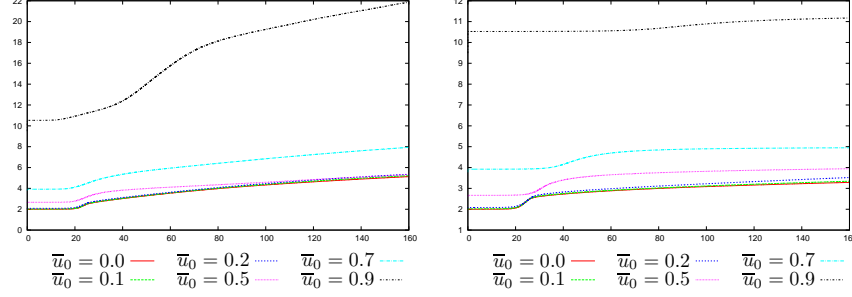
FIGURE 8. $E^{-1}(t)$ as a function of time, with constant mobility (left) and degenerate mobility (right), for $\varepsilon = \frac{1}{64\pi}$ and $\overline{u}_0 = \{0, 0.1, 0.2, 0.5, 0.7, 0.9\}$.

the boundary because of reduced mobility effects. In the constant mobility case, there is monotone decrease of $\beta_{int,0}^+/\beta_0^+$ with $\overline{u}_0$. In the degenerate mobility case, there is again monotone decrease of $\beta_{int,0}^+/\beta_0^+$ with $\overline{u}_0$ for $0 \le \overline{u}_0 \le 0.2$; however for $0.5 \le \overline{u}_0 \le 0.9$, $\beta_{int,0}^+/\beta_0^+$ is seen to increase with $\overline{u}_0$.

3.3. E^{-1}, $S(t)$, and $G(t)$. For $\varepsilon = \frac{1}{64\pi}$ and $\overline{u}_0 = \{0, 0.1, 0.2, 0.5, 0.7, 0.9\}$, the evolution of E^{-1} is portrayed in Figure 8, and the evolution of $S(t)$ is given in Figure 9. Monotone increase in $E^{-1}(t)$ with $\overline{u}_0$ can be seen in Figure 8 for both constant and degenerate mobility. The plots of $E^{-1}(t)$ as a function of time can be seen to contain a short flat initial segment, whose length decreases with $\overline{u}_0$ when the mobility is constant and whose length increases with $\overline{u}_0$ when the mobility is degenerate, followed by a short period with sharp increase, with continued increase there afterward. In Figure 9, monotone increase in $S(t)$ with $\overline{u}_0$ can be seen for the case of constant mobility, with some variation when $\overline{u}_0 \approx 0.2$. For the case of degenerate mobility, $S(t)$ can be seen in Figure 9 to increase with increasing $\overline{u}_0$ until $\overline{u}_0 \approx 0.2$, and then to decrease as $\overline{u}_0$ further increases. The plots of $S(t)$ can all be seen to contain an initial segment where the value of $S(t)$ is negligible, followed by a short period with sharp increase, with continued increase afterwards. Again, the length of the initial segment can be seen to decrease with $\overline{u}_0$ when the mobility is constant, and increase with $\overline{u}_0$ when the mobility is degenerate. Some transition of sorts in both $E^{-1}(t)$ and $S(t)$ can be seen to occur when $0.2 < \overline{u}_0 < 0.5$.

It follows from (3) that $E(0) = \frac{1}{2}(1 - \overline{u}_0^2) + O(\theta^2)$ when $u(x, 0) = \overline{u}_0 + \theta \mathcal{U}(-1, 1)$, and hence $E^{-1}(0)$ depends strongly on $\overline{u}_0$. To minimize this effect we have plotted the evolution of $E^{-1}(t)/E^{-1}(0)$ as a function of time for $\varepsilon = \frac{1}{64\pi}$ and $\overline{u}_0 = \{0, 0.1, 0.2, 0.5, 0.7, 0.9\}$ in Figure 10. Rescaled in this fashion, a transition of sorts can still be seen to occur when $0.2 < \overline{u}_0 < 0.9$. For the run with $\overline{u}_0 = 0.9$, there is an initial rapid decrease of the initial energy, which is why $E^{-1}(\approx 0)/E^{-1}(0)$ in this case is not close to 1. When plotting the graphs for the rescaled time $\tilde{t} = t/\overline{t}$ discussed in the Introduction (and the Appendix), a self-similarity of sorts seems to be apparent for $0 \le \overline{u}_0 \le 0.7$.

The evolution of $G(t) = E(t) - \frac{1}{2}(1 - S(t))$ for $\overline{u}_0 = \{0, 0.1, 0.2, 0.5, 0.7, 0.9\}$ and $\varepsilon = \frac{1}{64\pi}$ is displayed in Figure 11. Note that $G(0) = E(0) - \frac{1}{2}(1 - S(0)) \approx -\frac{1}{2}\overline{u}_0^2$, as can be seen in Figure 11. Since $G(t)$ depends linearly on $E(t)$ and $S(t)$, and $E(t)$ and $S(t)$ both contain linear segments, clearly $G(t)$ should also contain a
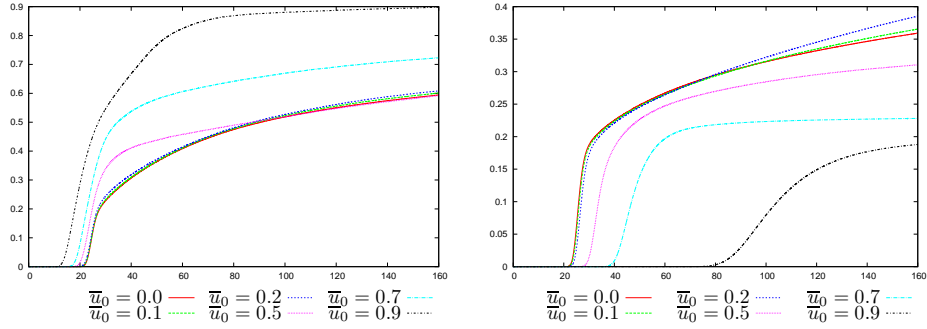
FIGURE 9. $S(t)$ as a function of time, with constant mobility (left) and degenerate mobility (right), for $\varepsilon = \frac{1}{64\pi}$ and $\overline{u}_0 = \{0, 0.1, 0.2, 0.5, 0.7, 0.9\}$.
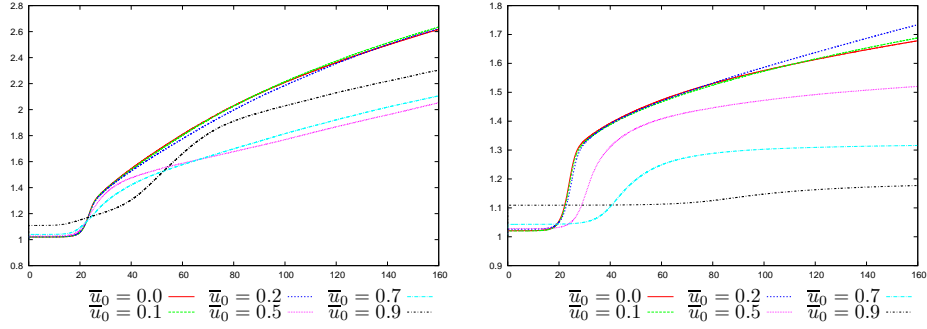

FIGURE 10. $E^{-1}(t)/E^{-1}(0)$ as a function of time for $\overline{u}_0 = \{0, 0.1, 0.2, 0.5, 0.7, 0.9\}$ and $\varepsilon = \frac{1}{64\pi}$, with constant mobility (left) and degenerate mobility (right).
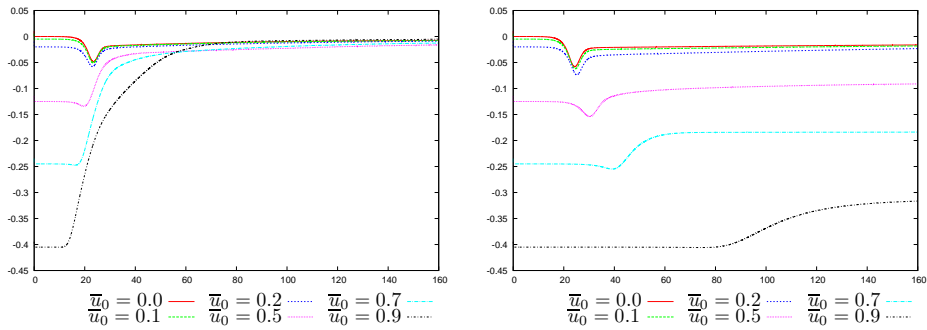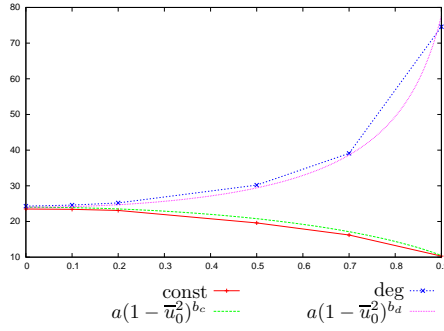

FIGURE 11. The evolution of $G(t)$ as a function of time, for $\overline{u}_0 = \{0, 0.1, 0.2, 0.5, 0.7, 0.9\}$ and $\varepsilon = \frac{1}{64\pi}$, with constant mobility (left) and degenerate mobility (right).

$\overline{u}_0$	constant	degenerate
0	23.5	24.3
0.1	23.4	24.6
0.2	23.1	25.2
0.5	19.6	30.2
0.7	16.2	39.1
0.9	10.3	74.6

TABLE 1. Crossover times t_{cross} for $G(t) = E(t) - \frac{1}{2}(1 - S(t))$.

FIGURE 12. Crossover time t_{cross} versus $\overline{u}_0$ for constant and degenerate mobility fitted by $a(1 - \overline{u}_0^2)^{b_c}$ and $a(1 - \overline{u}_0^2)^{b_d}$, respectively. Here $a = 24$, $b_c = \frac{1}{2}$ and $b_d = -0.707 \approx -2^{-\frac{1}{2}}$.

linear segment, as can also be seen. A unique minimum can be seen in these plots. We have identified the times t at which $\frac{d}{dt}[E(t) - \frac{1}{2}(1 - S(t))] = 0$ as "crossover times", and listed these times in Table 1. From Table 1 it can be clearly seen that the crossover times occur consistently later for the case of degenerate mobility compared to the case of constant mobility, with monotone decrease (increase) in the crossover times with increasing $\overline{u}_0$ for the case of constant (degenerate) mobility, with enhanced dependence on $\overline{u}_0$ for $\overline{u}_0 > 0.2$ in both cases. In Figure 12, the crossover times t_{cross} are compared with the best fitted plots of $a(1 - \overline{u}_0^2)^b$. Here we note that for the exponents b we obtain $b = \frac{1}{2}$ in the constant mobility case, and $b = -0.707 \approx -2^{-\frac{1}{2}}$ in the degenerate mobility case. The precise dynamic interpretation of t_{cross} is not completely obvious; however before t_{cross}, $-\frac{d}{dt}E > \frac{1}{2}\frac{d}{dt}S$ and energy decrease dominates saturation, and after t_{cross}, $\frac{1}{2}\frac{d}{dt}S > -\frac{d}{dt}E$ and saturation slowly continues with less actual energy decrease. In Fig. 13, the ratio $\beta_{int,0}^+/\beta_0^+$ is portrayed for various values of $\overline{u}_0$ and crossover times have been indicated. At late times $\beta_{int,0}^+/\beta_0^+ \ll 1$ and the boundary components $\beta_{bdy,0}^+$ are predominant in β_0^+. All of these plots, except for $\overline{u}_0 = 0.9$ in the degenerate case, can be seen to contain an interim regime during which monotonicity is reversed, and crossover can be seen during this regime.

3.4. **The linear regime and dependence on the amplitude of the initial perturbation.** In order to understand the effect of the amplitude of the initial perturbation on our solutions, we compare results for $\theta = 5 \times 10^{-2}$, 5×10^{-3}, 5×10^{-5}, $\varepsilon = 1/64\pi$, $\overline{u}_0 = 0$ for $E(t)^{-1}$ and $S(t)$ in Figure 14. Since the influence
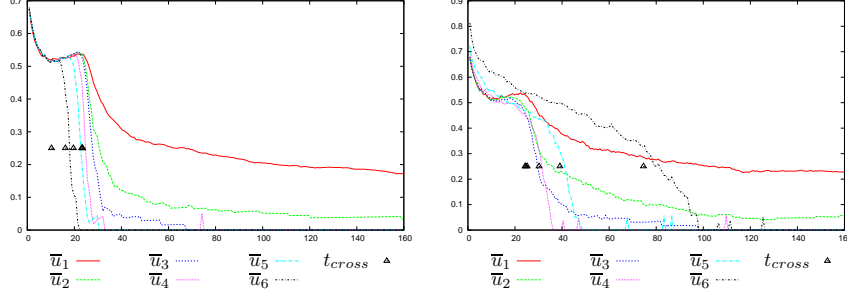
FIGURE 13. The evolution of $\beta_{int,0}^+/\beta_0^+$ as a function of time, for $\overline{u}_0 = \{\overline{u}_k, \ k = 1, \ldots, 6\} = \{0, 0.1, 0.2, 0.5, 0.7, 0.9\}$ and $\varepsilon = \frac{1}{64\pi}$, with constant mobility (left) and degenerate mobility (right) with crossover time t_{cross}.
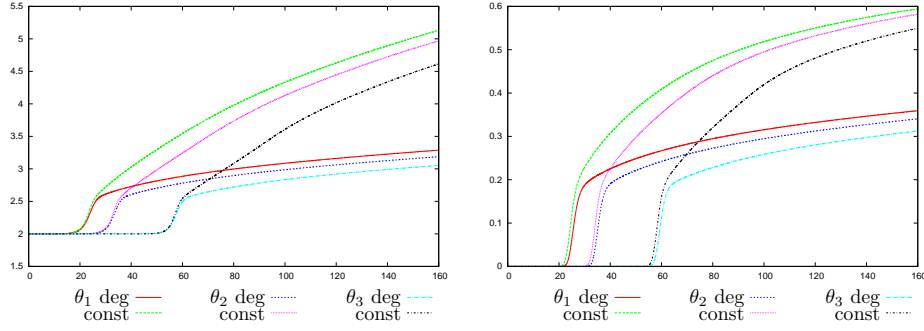

FIGURE 14. Time evolution of $E(t)^{-1}$ (left) and $S(t)$ (right), for $\overline{u}_0 = 0$ and $\theta = \{\theta_1, \theta_2, \theta_3\} = \{5 \times 10^{-2}, 5 \times 10^{-3}, 5 \times 10^{-5}\}$.

of the initial amplitude can perhaps be expected to be most substantial during the initial stages of evolution, let us consider solutions of the form

$$u(x,t) = \frac{A_0(t)}{2} + \sum_{m,n=1}^{\infty} A_{mn}(t)\cos(m\pi x_1)\cos(n\pi x_2),$$

which satisfy the boundary conditions as we have chosen $H = 1$. For the initial conditions described in Section 2.2, within the framework of linear theory, we set

$$u(x,t) \approx \overline{u}_0 + \theta \sum_{m,n=1}^{\infty} a_{nm} e^{\sigma_{nm} t} \cos(m\pi x_1)\cos(n\pi x_2), \tag{13}$$

where $|a_{nm}| \leq 1$ and $\sigma_{nm} = M(\overline{u}_0)(1 - \varepsilon^2(m^2 + n^2)\pi^2)((m^2 + n^2)\pi^2) \leq \sigma_{fastest} = \frac{M(\overline{u}_0)}{4\varepsilon^2}$, with $\sigma_{fastest}$ being attained when $|\vec{k}_{fastest}|^2 = (m^2 + n^2)\pi^2 = (2\varepsilon^2)^{-1}$. Hence, modulo the obvious limitations of linear theory, for $0 \leq \overline{u}_0 < 1$ saturation cannot occur prior to time $t = t_{linear}$ at which $1 = \overline{u}_0 + \theta e^{\frac{M(\overline{u}_0)}{4\varepsilon^2} t_{linear}}$. For solutions of the form (13), $4\pi\varepsilon$, its spatial period, acts as a length scale during the linear regime. More generally, if the solution is not constrained to be of the precise form (13), then $2\pi/|\vec{k}_{fastest}| = 2^{\frac{3}{2}}\pi\varepsilon$ provides an indication of the dominant length scales in the system.

θ	t_{linear}	$\hat{t}_{linear}$ (constant)	$\hat{t}_{linear}$ (degenerate)
5×10^{-2}	12	18.2	19.4
5×10^{-3}	21.2	28.5	29.6
5×10^{-5}	39.6	51.8	53.2

TABLE 2. Estimated time $\hat{t}_{linear}$ based on the length of flat segments of $S(t)$.

Thus

$$t_{linear} = \frac{4\varepsilon^2}{M(\overline{u}_0)} \ln\Big(\frac{1 - \overline{u}_0}{\theta}\Big) \tag{14}$$

constitutes a (naïve) linear estimate for the end of the linear regime and the initiation of saturation. It follows from (14) that for three different values, θ_i, $i \in \{1, 2, 3\}$, of the initial amplitude, the associated times t_{linear}^i, $i \in \{1, 2, 3\}$, should satisfy

$$\mathcal{A} = \frac{\ln(\theta_2) - \ln(\theta_1)}{\ln(\theta_3) - \ln(\theta_2)} = \frac{t_{linear}^2 - t_{linear}^1}{t_{linear}^3 - t_{linear}^2}. \tag{15}$$

From the definition of $S(t)$, clearly prior to initiation of saturation, $S(t)$ should be negligible, as we saw in Section 3.3. From the definition of $E(t)$, it follows from (13) and linear theory, that $E(t)$ (and $E^{-1}(t)$) should appear to be fairly flat and roughly equal to its initial value $E_{linear}(t) = \frac{1}{2}(1 - \overline{u}_0^2) + O(\theta^2)$, for $0 \le t < t_{linear}$, if not for an indeed somewhat more extended interval [46, 40]. See for example Figure 14, where the linear portion of $E^{-1}(t)$ can be seen to end at $t \approx 20$ even though $t_{linear} \approx 12$ for $\overline{u}_0 = 0$, $\theta = 5 \times 10^{-2}$, $\varepsilon = \frac{1}{64\pi}$. Equation (15) can be roughly verified based on the lengths of the flat segments of $S(t)$ ($\hat{t}_{linear} = \min\{t | S(t) \ge tol_S\}$) in Figure 14, which we have recorded in Table 2. While the theoretical value of $\mathcal{A}$ is 0.5, the computed values can be seen from Table 2 to correspond to $\mathcal{A} \approx 0.44$ (constant mobility) and $\mathcal{A} \approx 0.43$ (degenerate mobility).

For the case of constant mobility, for the deep quench obstacle problem, there should be no nonlinear effects prior to the onset of saturation, which should occur after t_{linear}, so the fastest growing mode should initially be well approximated by $|\vec{k}_{fastest}| = (\sqrt{2}\varepsilon)^{-1}$. This would imply $2^{\frac{3}{2}}\pi\varepsilon$ as a length scale estimate during the linear regime.

As mentioned earlier, $\frac{\varepsilon\pi}{2} \frac{1}{E(t)}$ should scale with the dominant length scale of the system. If more specific assumptions are made on the structure of the solution, such as that the system is divided into identical square periodic units where $u \equiv \pm 1$ which contain an embedded circular region where $u \equiv \mp 1$, then when $\overline{u}_0 = 0$, $\frac{\varepsilon\pi^2}{\sqrt{2\pi}} \frac{1}{E(t)}$ provides an estimate for the dominant (spatial period) length scale of the system. Based on either of these criteria, during the first stages of evolution when $E^{-1}(t)$ is roughly flat, the length scale of the system can be seen from Figure 14 to be in rough agreement with the length scale predictions of linear theory.

The dominant length scale in the system can be roughly estimated by $(\beta_0^+)^{-\frac{1}{2}}$, $(\beta_{int,0}^+)^{-\frac{1}{2}}$, and $4(\beta_{bdy,0}^+)^{-\frac{1}{2}}$, see Figure 15. The depicted results for $(\beta_{int,0}^+)^{-\frac{1}{2}}$ are in good qualitative agreement with E^{-1} as a length scale indicator, see Figure 3 (left). Based on $(\beta_{int,0}^+)^{-\frac{1}{2}}$, the dominant length scale can be seen to increase rapidly during an initial transient period, which lasts roughly until about time $t \approx \frac{1}{2}t_{linear}$. Afterwards, there is a period during which the length scale of the system does not
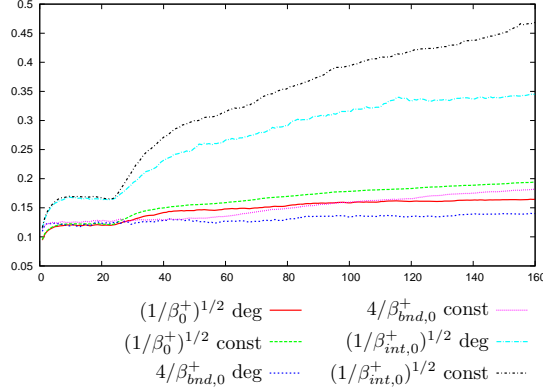
FIGURE 15.   Evolution of $(\beta_0^+)^{-\frac{1}{2}}$, $4(\beta_{bdy,0}^+)^{-1}$ and $(\beta_{int,0}^+)^{-\frac{1}{2}}$ over time with degenerate and constant mobility for $\overline{u}_0 = 0$, $\varepsilon = \frac{1}{64\pi}$.

change drastically, as can be seen in the relative steadiness of the various Betti numbers, see Figure 15. Note that during this period, the dominant length scale as evaluated based on $(\beta_{int,0}^+)^{-\frac{1}{2}} \approx 0.17$ and $(\beta_0^+)^{-\frac{1}{2}} \approx 0.12$ (see Figure 4) can be seen to be considerably more than the length scale implied by linear theory. This may reflect both the relatively small size of the systems studied, as well as the structure and relatively high degree of connectivity of the solution components as can be seen for example in Figure 1.

For the case of degenerate mobility, nonlinear slowing should affect the evolution, so it would be reasonable to expect the onset of saturation to occur after t_{linear}, as reflected in the lengthened linear segments in $E^{-1}(t)$ and $S(t)$, as noted earlier in Section 3.3. Based on an examination of the Betti numbers, we can see qualitatively similar evolutions of the length scales during the early stages as in the constant mobility case; i.e. an initial period with rapid decrease in β_0^+ and $\beta_{int,0}^+$ until a relatively constant level is reached for β_0^+ and $\beta_{int,0}^+$, with the dominant length scale in the system based on the Betti numbers being again significantly larger than the length scale predicted by the fastest growing mode. See Figure 2.

3.5. **Power laws.** As discussed in the introduction, various considerations have led power law behavior to be expected of the form $at^b + c$ for the dominant length scale, and in particular we are interested in the exponent b. Plotting graphs of $E^{-1}(t)$ in the log-log scale confirms that the evolution takes on the form of a power law after some time, see Figure 16. Looking at Figure 19, below, three regimes could be identified: a) a short period of initial evolution, with roughly the same exponent for both mobilities b) followed by an evolution with exponent $> 1/3$ for constant mobility and $< 1/4$ for degenerate mobility c) then apparently the predicted evolution with $1/3$, $1/4$ growth. The constant mobility seems to be growing faster than the $1/3$ upper bound, which potentially could be attributed to boundary effects. The degenerate mobility is approaching the $1/4$ growth rate. The differences are less apparent if pictures are plotted in normal scale (non-log).

In Figure 17 we plot the quantity $S(\check{t}, t; r, \varphi)$ from [36, 41] and the Appendix, for $\varphi = 1$,

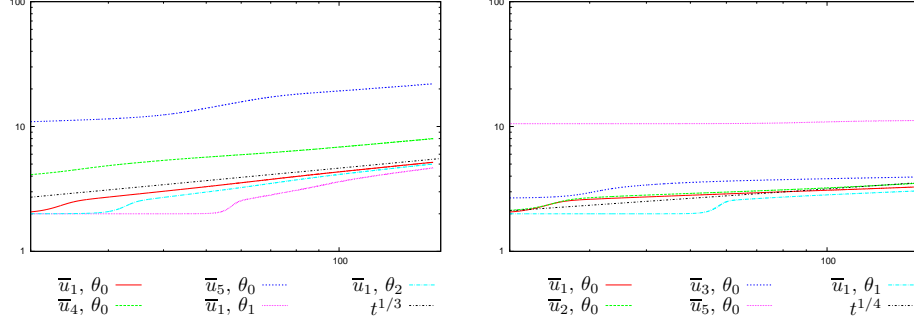$$S(\check{t}, t; r, 1) := (t - \check{t})^{-1/r} \|E(t)\|_{L^r([\check{t}, t])},$$

FIGURE 16. Log-scale plot of $E^{-1}(t)$ for $\overline{u}_0 = \{\overline{u}_k,\, k = 1, 2, 3, 4, 5\} = \{0, 0.2, 0.5, 0.7, 0.9\}$ ($\theta = \{\theta_0, \theta_1, \theta_2\} = \{5 \times 10^{-2}, 5 \times 10^{-5}, \theta = 5 \times 10^{-3}\}$), constant mobility (left) and degenerate mobility (right).
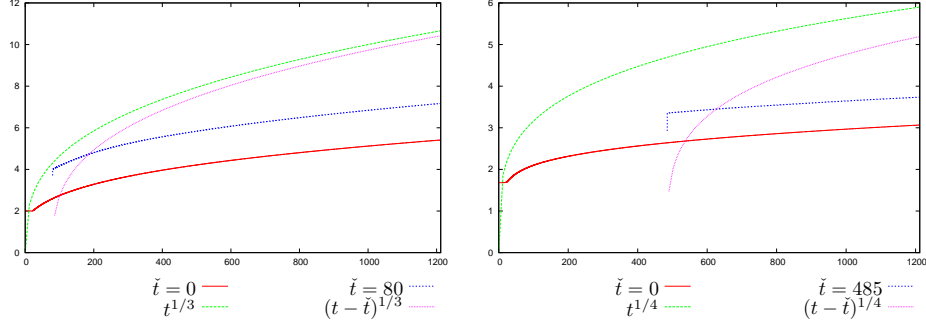

FIGURE 17. $1/S(\check{t}, t; r, 1)$ and $(t - \check{t})^{1/r}$ for constant (left) and degenerate (right) mobility for $\check{t} = 0, t^*$.

for $\check{t} \leq t \leq T$ with $\overline{u}_0 = 0$. We set $r = 1/3$ for the constant mobility and $r = 1/4$ for the degenerate mobility. The time $\check{t}$ corresponds to the times 0 and t^*, where t^* is the time such that $E(t^*) = \frac{1}{4}(1 - \overline{u}_0^2)$; for the constant mobility $t^* \approx 80$ and for the degenerate mobility $t^* \approx 485$.

If we choose to try to compare our results with the scaled upper bounds for coarsening given in (6)–(8), the results appear to be relatively more successful, at least for $0 \leq \overline{u}_0 \leq 0.7$. See Figure 18, where we plot $E^{-1}(t)$ and the predicted upper bounds on a log timescale. The case $\overline{u}_0 = 0.9$ corresponds to the "small volume fraction limit" $\phi := (1 - \overline{u}_0)/2 \ll 1$, where logarithmic corrections to the scaling may be needed [16]. We remark that the analysis in [16] does not apply directly to the deep quench context, particularly in the case of degenerate mobility.

In Figure 19, (single run) log-scale plots of $E(t)^{-1}$ and $E(t) - 0.5(1 - S(t))$ are displayed, reflecting a similar long time interval. We can see that at these late times, the scaling laws are by now holding fairly well for $E^{-1}(t)$ and the system is pretty well saturated. We also include plots of u at late times. It seems to take slightly longer for the scaling laws to take effect when $\overline{u}_0$ is larger. Such a tendency was also reported in [26] where a numerical study of E^{-1} for the Cahn–Hilliard equation with constant mobility was performed which focused on the nucleation
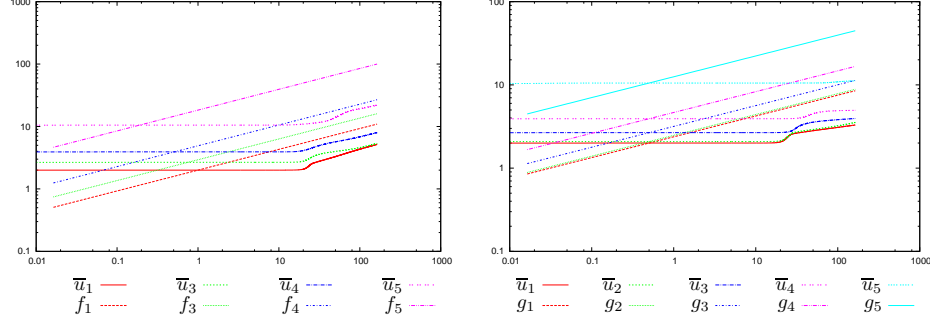
FIGURE 18. Log-scale plots of E^{-1} and $f_k(t) = 2(2t)^{1/3}/(1-\overline{u}_k^2)^{4/3}$ versus time for constant mobility (left), and E^{-1} and $g_k(t) = 2(2t)^{1/4}/(1 - \overline{u}_k^2)$ versus time degenerate mobility (right) for $\overline{u}_0 = \{\overline{u}_1, \overline{u}_2, \overline{u}_3, \overline{u}_4, \overline{u}_5\} = \{0, 0.2, 0.5, 0.7, 0.9\}$.
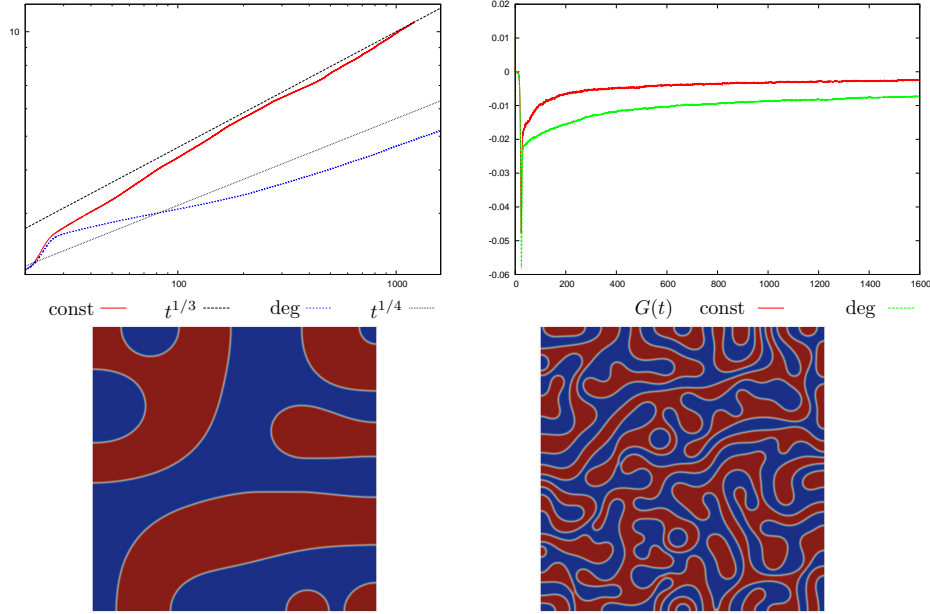

FIGURE 19. Long time log-scale plot of $E^{-1}(t)$ (left) and $G(t) = E(t) - 0.5(1 - S(t))$ (right) over the time interval $[0, 1600]$ for constant and degenerate mobilities, with $\overline{u}_0 = 0$ (single run). The bottom row shows the computed solution u at time $t = 1600$ for constant (left) and degenerate (right) mobilities.

regime, but here it is only a small effect. We present the results from a run with $\overline{u}_0 = 0.9$ in Figure 20, where we show plots of $E(t)^{-1}$ for a single run over a long time interval. As before, we also visualize u at late times. It could be seen that in the case of degenerate mobility a steady state has been reached from around half-way through the simulation, while in the constant mobility case the coarsening was still continuing at time $t = 1600$.
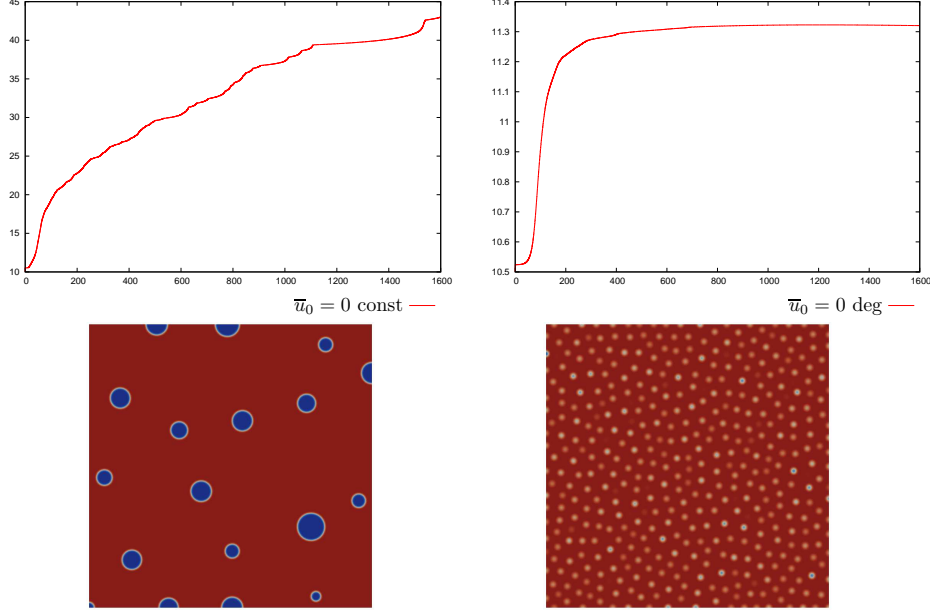
FIGURE 20. Long time plot of $E^{-1}(t)$ over the time interval $[0, 1600]$ for constant (left) and degenerate (right) mobilities, with $\overline{u}_0 = 0.9$ (single run). The bottom row shows u at time $t = 1600$ for constant (left) and degenerate (right) mobilities.

3.6. **The structure function.** In this section we would like to test the hypothesis in [24] that for phase separation models such as Cahn–Hilliard, at sufficiently large times, the circularly averaged structure function can be expressed as

$$\mathbf{S}(k, t) \approx \mathbf{S}(K(t), t) F(k/K(t)) \approx K^{-2}(t)\widetilde{F}(k/K(t)),$$

where $K(t)$ is the value of k at which $\mathbf{S}(k, t)$ attains its maximum and $F(\cdot)$, $\widetilde{F}(\cdot)$ are scale invariant functions. Thus it seems of interest to calculate $K^2(t)\mathbf{S}(k, t)$ as a function of $k/K(t)$, in order to verify the degree to which the scale invariant hypothesis is fulfilled.

In the computational experiments, it was observed that the dominant frequency $K(t)$ plays a role in the scaling. Moreover, $K^{-1}(t)$ provides an additional measure of the typical length scales of the system, and hence one would expect that $2\pi K^{-1}(t) \approx l(t)$, where $l(t)$ corresponds to the typical length scale of the system as discussed earlier.

However, since we are using discrete FFT, $K(t)$ only attains discrete values and is discontinuous in time. Therefore the graphs will not be properly "centered" if one uses $K^{-1}(t)$ in evaluating $K^2(t)\mathbf{S}(k, t)$. To circumvent this difficulty, we assumed that $\mathbf{S}(K(t), t) \propto K^{-2}(t)$, and accordingly computed $\mathbf{S}(k, t)[R(t)]^{-2}$ as a function of $kR(t)$ where $R(t) := (\mathbf{S}(K(t), t))^{-1/2}$.

In Figures 21–23, we have displayed the scaled structure function, $\mathbf{S}(k, t)[R(t)]^{-2}$, as a function of $kR(t)$, for $\overline{u}_0 = 0, 0.5, 0.9$. We observe that the scaling is not attained at $t = 40.8$. The scaling invariance seems to be better for the case of constant mobility when $\overline{u}_0 = 0$ and 0.9, and better for the case of degenerate mobility when
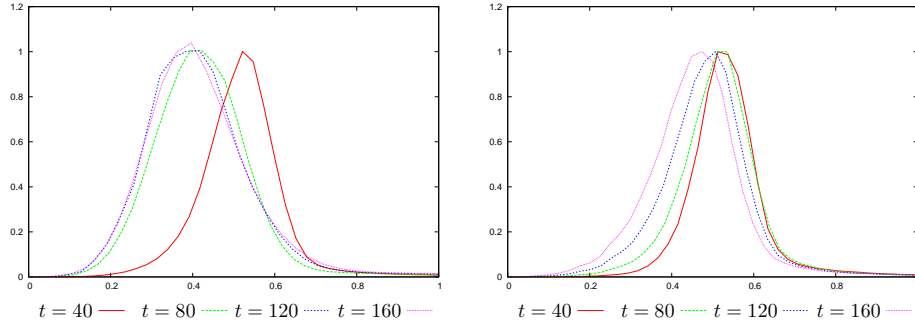
FIGURE 21. $\mathbf{S}(k,t)[R(t)]^{-2}$ vs. $kR(t)$ for $t = 40, 80, 120, 160$, and $\overline{u}_0 = 0$, with constant (left) and degenerate mobility (right).

FIGURE 22. $\mathbf{S}(k,t)[R(t)]^{-2}$ vs. $kR(t)$ for $t = 40, 80, 120, 160$, and $\overline{u}_0 = 0.5$, with constant (left) and degenerate mobility (right).
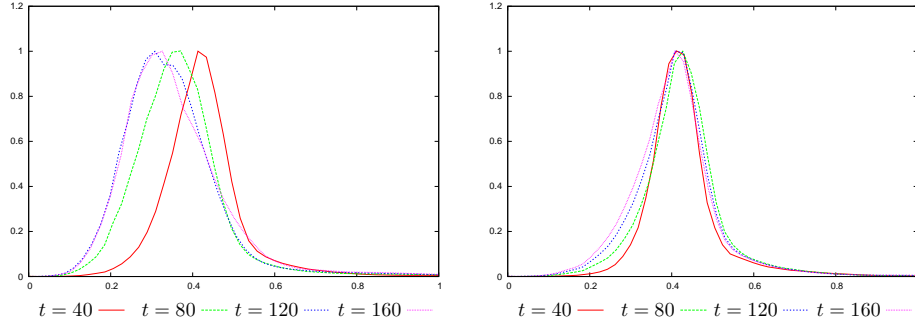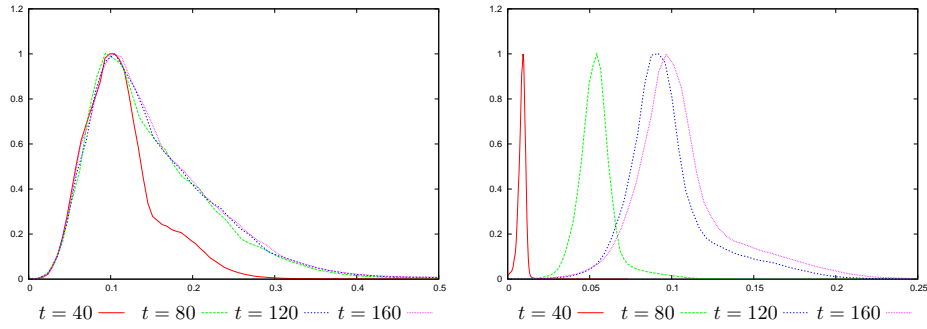

FIGURE 23. $\mathbf{S}(k,t)[R(t)]^{-2}$ vs. $kR(t)$ for $t = 40, 80, 120, 160$, and $\overline{u}_0 = 0.9$, with constant (left) and degenerate mobility (right).

$\overline{u}_0 = 0.5$. A long time computation for a single realization of the initial condition seemed to indicate that at longer times, the scaling is approximately attained for both constant and degenerate mobilities.

4. **Summary and conclusions.** A series of numerical computations were undertaken for the deep quench obstacle problem for both constant and degenerate mobilities for a variety of mean masses. In the computations the initial conditions were taken as a perturbation of the mean mass. Because for the deep quench obstacle problem there is no binodal and all of the masses $-1 < \overline{u}_0 < 1$ studied were "subspinodal", in other words linearly unstable, phase separation was seen to ensue. Roughly speaking, the phase separation was seen to proceed via an initial stage prior to saturation marked by linear growth, a transitional period, and finally a coarsening period. By postprocessing the results of the computations based on a number of benchmarks, we were able to gain new insight into the details of the transitional period and to verify new scaled upper coarsening bounds.

During the initial period, the evolution was similar for the constant and the degenerate mobilities and for all the various mean masses studied, and the plots of $E(t)$, $S(t)$, and $G(t)$ appeared to be roughly flat. While the duration of the linear regime appeared to be longer than indicated by linear theory, as has been predicted previously in the context of the Cahn–Hilliard equation with constant mobility, the relative length of the linear regimes could be seen to be roughly proportional to the various linear growth rates based on the amplitudes of the initial perturbations. During the beginning of the linear regime, the Betti numbers exhibited rapid decrease before reaching a roughly constant level.

The exact onset of the transitional period seemed to depend somewhat on the benchmark considered. Before rapid growth in $E(t)$, $S(t)$, and $G(t)$ occurred, already a change in monotonicity of the Betti numbers could be seen, indicating a short period of increase in the number of connected components. Sometime during this period of inverted monotonicity, a period of rapid growth in $E^{-1}(t)$ and $S(t)$ was seen to occur. Over the entire period of the evolution, $G(t)$ was seen to have a unique minimum which occurred during the period of rapid growth of $E^{-1}(t)$ and $S(t)$. The time at which this minimum was attained could thus be identified as a well-defined "crossover" time. These crossover times could be seen to depend on the type of mobility and were roughly linearly proportional to the mean mass. Sometime a bit after the crossover time, by inspecting the evolution of the Betti numbers, a dominance of the boundary components takes over. These details should help to unravel the mathematics of the dynamics of the transitional "reorganizational" phase.

Afterwards during coarsening, the results appeared to be in good accord with the predicted upper bounds based on rescaling the energy and time with mean mass dependent scalings, with the bounds appearing to hold even before the coarsening regime takes effect. Finally, the structure function exhibited approximate self-similar scaling in a number of long runs.

We point out that to the best of our knowledge, the functional $G(t)$ which we have defined constitutes a new benchmark which has yet to be implemented numerically or studied analytically for the deep quench obstacle problem or for similar Cahn–Hilliard type settings. We find it fascinating that we have identified a functional which seems to robustly exhibit a unique minimizer. Further investigation of the evolution of $G(t)$ and its interrelationship with the other benchmarks seems clearly called for. Other possible areas of future research include extending the presented study to three space dimensions, as well as using more sophisticated tools from computational algebraic topology.

5. **Appendix.** The bounds (6)–(8), which are in the spirit of [36, 43], can be derived from Lemmas 1-4 and Corollary 1 in [41] by rescaling $E(t)$, $L(t)$, and t, and by deriving a simple inequality.

More specifically, setting $\widetilde{E}(\tilde{t}) := \frac{1}{\overline{E}}E(t)|_{\tilde{t}:=t/\overline{t}}$, $\widetilde{L}(\tilde{t}) := \frac{1}{\overline{L}}L(t)|_{\tilde{t}:=t/\overline{t}}$, $\tilde{t} := t/\overline{t}$ in [41, Lemma 1], where $\overline{L}$ and $\overline{t}$ denote scaling constants to be determined and $\overline{E} = \frac{1-\overline{u}^2}{2}$, we have

Lemma 5.1. *If* $|\bar{u}| < 1$, *then* $1 \leq 2^{3/2}[3\left(\widetilde{E}(\tilde{t}) + \frac{2\varepsilon|\partial\Omega|}{(1-\overline{u}^2)|\Omega|}\right)\frac{\overline{L}}{\overline{E}}\widetilde{L}(\tilde{t})]^{1/2} + \widetilde{E}(\tilde{t})$ *for* $\tilde{t} \geq 0$.

Defining $\tilde{t}^* := \sup\{\{0\} \cup \{\tilde{t} \in (0,\infty)|\widetilde{E}(\tilde{t}) \geq 1\}\}$ and noting that $\widetilde{E}_{\tilde{t}} \leq 0$, we obtain as in [41, Corollary 1],

Corollary 1. *If* $|\bar{u}| < 1$, *then neglecting boundary terms for the sake of simplicity,* (i) $\widetilde{E} \geq 1$ *if* $\tilde{t} \leq 1$, *and* (ii) $\widetilde{E} < 1$ *and* $\widetilde{E}\widetilde{L} \geq \frac{\overline{E}}{24\overline{L}}(1 - \widetilde{E})^2$ *if* $\tilde{t} > 1$. *Thus* $\widetilde{E}(\tilde{t})\widetilde{L}(\tilde{t}) \geq \widetilde{B}(\tilde{t}) \geq \widetilde{B}(\tilde{t}^*)$ *for* $\tilde{t} > \tilde{t}^*$, *where* $\widetilde{B}(\tilde{t}) := \frac{(1-\widetilde{E}(\tilde{t}))^2\,\overline{E}}{24\,\overline{L}}$ *and* $\widetilde{B}(\tilde{t}^*) = 0$ *if* $\tilde{t}^* > 0$.

By Cauchy–Schwarz, $\frac{1}{|\Omega|}\int_\Omega(1-u^2)\,\mathrm{d}x \leq (1-\overline{u}^2)$. Hence by (3), $\frac{1}{|\Omega|}\int_\Omega(1-u^2)\,\mathrm{d}x \leq (1-\overline{u}^2)\min\{1,\widetilde{E}(t)\}$. Proceeding now as in the proof of [41, Lemmas 2, 3],

Lemma 5.2. *Suppose that* $|\bar{u}| < 1$. *Then* $|\widetilde{L}_{\tilde{t}}|^2 \leq -\widetilde{E}_{\tilde{t}}$ *for (DQ) with nondegenerate mobility and* $\overline{t} := \frac{\varepsilon^2\overline{L}^2}{\overline{E}}$, *and* $|\widetilde{L}_{\tilde{t}}|^2 \leq -\min\{1, \widetilde{E}\}\widetilde{E}_{\tilde{t}}$ *for (DQ) with degenerate mobility and* $\overline{t} := \frac{\varepsilon^2\overline{L}^2}{2\overline{E}^2}$.

From Corollary 2, Lemma 2 and [41, Lemma 4], it follows in terms of the original variables for $t > t^*$ where $t^* := \sup\{\{0\} \cup \{t \in (0,\infty)|E(t) \geq \frac{1}{2}(1 - \overline{u}^2)\}\}$, that for the case of nondegenerate mobility,

$$S^{-1}(0,t;r,\varphi) \leq \overline{E}^{-\varphi}\overline{L}^{(1-\varphi)}\left(\frac{\overline{E}t}{\varepsilon^2\overline{L}^2}\right)^{\frac{1}{3}}\left[\vartheta_1 - \left(\frac{L^3(0)\varepsilon^2}{\overline{E}\overline{L}t}\right)^{\frac{3-r}{3}}\right]^{-1/r}, \qquad (16)$$

where $0 \leq \varphi \leq 1$, $(1-\varphi)r < 2$, $r < 3$, $\varphi r > 1$, and for the case of degenerate mobility,

$$S^{-1}(0,t;r,\varphi) \leq \overline{E}^{-\varphi}\overline{L}^{(1-\varphi)}\left(\frac{2\overline{E}^2 t}{\varepsilon^2\overline{L}^2}\right)^{\frac{1}{4}}\left[\vartheta_2 - \left(\frac{L^4(0)\varepsilon^2}{2(\overline{E}\overline{L})^{\frac{1}{2}}\,t}\right)^{\frac{4-r}{4}}\right]^{-1/r}, \qquad (17)$$

where $0 \leq \varphi \leq 1$, $(1-\varphi)r < 2$, $r < 4$, $\varphi r > 2$, and $\vartheta_i = \vartheta_i(\varphi, r)$ for $i \in \{1, 2\}$, see [41, 43]. Note that (16)–(17) correspond to (6)–(7). As explained in [41, 43], somewhat similar bounds maybe be prescribed for times $0 < t < t^*$, but they are not so relevant to the present context where $E(0) \approx \frac{1}{2}(1 - \overline{u}^2)$.

The bounds (16)–(17) may now be evaluated when $\overline{L} = \overline{E} = \frac{1}{2}(1-\overline{u}^2)$. Although (16)–(17) provide upper bounds for all times $t > t^*$, at large times the form of the upper bounds simplifies somewhat. By considering the estimates for large t, and evaluating these upper bounds for large t in the limit when $\varphi \to 1$, $r \to 3+\alpha$ where $\alpha = 0$ in the nondegenerate case and $\alpha = 1$ in the degenerate case, and noting that in this parameter limit $\vartheta_i \to 1$ for $i \in \{1, 2\}$ (see [41]), the approximate upper bounds prescribed in (8)–(9) now follow.

The rescalings have been chosen to make the statement of the results as simple as possible, and in this sense our approach is somewhat similar to the approach adopted by Conti et al. [16].

REFERENCES

[1] N. D. Alikakos, P. W. Bates and X. F. Chen, *Convergence of the Cahn–Hilliard equation to the Hele–Shaw model*, Arch. Rational Mech. Anal., **128** (1994), 165–205.

[2] N. D. Alikakos, G. Fusco and G. Karali, *Motion of bubbles towards the boundary for the Cahn–Hilliard equation*, European J. Appl. Math., **15** (2004), 103–124.

[3] C. H. Arns, M. A. Knackstedt, W. V. Pinczewski and K. R. Mecke, *Euler–Poincaré characteristics of classes of disordered media*, Phys. Rev. E, **63** (2001), 031112.

[4] Ľ. Baňas and R. Nürnberg, *Finite element approximation of a three dimensional phase field model for void electromigration*, J. Sci. Comp., **37** (2008), 202–232.

[5] Ľ. Baňas and R. Nürnberg, *A multigrid method for the Cahn–Hilliard equation with obstacle potential*, Appl. Math. Comput., **213** (2009), 290–303.

[6] Ľ. Baňas and R. Nürnberg, *Phase field computations for surface diffusion and void electromigration in $\mathbb{R}^3$*, Comput. Vis. Sci., **12** (2009), 319–327.

[7] J. W. Barrett and J. F. Blowey, *An error bound for the finite element approximation of the Cahn–Hilliard equation with logarithmic free energy*, Numer. Math., **72** (1995), 1–20.

[8] J. W. Barrett, J. F. Blowey and H. Garcke, *Finite element approximation of the Cahn–Hilliard equation with degenerate mobility*, SIAM J. Numer. Anal., **37** (1999), 286–318.

[9] J. W. Barrett, R. Nürnberg and V. Styles, *Finite element approximation of a phase field model for void electromigration*, SIAM J. Numer. Anal., **42** (2004), 738–772.

[10] J. F. Blowey and C. M. Elliott, *The Cahn–Hilliard gradient theory for phase separation with non-smooth free energy. Part I: Mathematical analysis*, European J. Appl. Math., **2** (1991), 233–280.

[11] J. F. Blowey and C. M. Elliott, *The Cahn–Hilliard gradient theory for phase separation with non-smooth free energy. Part II: Numerical analysis*, European J. Appl. Math., **3** (1992), 147–179.

[12] J. W. Cahn, *On spinodal decomposition*, Acta Metall., **9** (1961), 795–801.

[13] J. W. Cahn, C. M. Elliott and A. Novick-Cohen, *The Cahn–Hilliard equation with a concentration dependent mobility: Motion by minus the Laplacian of the mean curvature*, European J. Appl. Math., **7** (1996), 287–301.

[14] J. W. Cahn and J. E. Hilliard, *Free energy of a non-uniform system. I. Interfacial free energy*, J. Chem. Phys., **28** (1958), 258–267.

[15] X. Chen, *Global asymptotic limit of solutions of the Cahn–Hilliard equation*, J. Differential Geom., **44** (1996), 262–311.

[16] S. Conti, B. Niethammer and F. Otto, *Coarsening rates in off-critical mixtures*, SIAM J. Math. Anal., **37** (2006), 1732–1741.

[17] M. I. M. Copetti and C. M. Elliott, *Numerical analysis of the Cahn–Hilliard equation with a logarithmic free energy*, Numer. Math., **63** (1992), 39–65.

[18] R. Dal Passo, L. Giacomelli and A. Novick-Cohen, *Existence for an Allen-Cahn/Cahn-Hilliard system with degenerate mobility*, Interfaces Free Bound., **1** (1999), 199–226.

[19] C. M. Elliott and D. A. French, *Numerical studies of the Cahn–Hilliard equation for phase separation*, IMA J. Appl. Math., **38** (1987), 97–128.

[20] C. M. Elliott and H. Garcke, *On the Cahn–Hilliard equation with degenerate mobility*, SIAM J. Math. Anal., **27** (1996), 404–423.

[21] C. M. Elliott and S. Luckhaus, *A generalized diffusion equation for phase separation of a multi-component mixture with interfacial free energy* (1991), IMA, Univ. of Minnesota, Preprint 887.

[22] C. M. Elliott and S. Zheng, *On the Cahn–Hilliard equation*, Arch. Rational Mech. Anal., **96** (1986), 339–357.

[23] P. Fratzl and J. L. Lebowitz, *Universality of scaled structure functions in quenched systems undergoing phase separation*, Acta Metall., **37** (1989), 3245–3248.

[24] P. Fratzl, J. L. Lebowitz, O. Penrose and J. Amar, *Scaling functions, self-similarity, and the morphology of phase-separating systems*, Phys. Rev. B, **44** (1991), 4794–4811.

[25] M. Gameiro, K. Mischaikow and T. Wanner, *Evolution of pattern complexity in the Cahn–Hilliard theory of phase separation*, Acta Mater., **53** (2005), 693–704.

[26] H. Garcke, B. Niethammer, M. Rumpf and U. Weikard, *Transient coarsening behaviour in the Cahn–Hilliard model*, Acta Mater., **51** (2003), 2823–2830.

[27] J. D. Gunton, M. San Miguel and P. S. Sahni, *The dynamics of first-order phase transitions*, in "Phase Transitions and Critical Phenomena," **8**, Academic Press, London (1983), 267–482.

[28] R. Hilfer, *Review on scale dependent characterization of the microstructure of porous media*, Transp. Porous Media, **46** (2002), 373–390.

[29] J. E. Hilliard, *Spinodal decomposition*, in "Phase Transformations" (ed. H. I. Aaronson), American Society for Metals, Metals Park, Ohio, 497–560.

[30] D. J. Horntrop, *Concentration effects in mesoscopic simulation of coarsening*, Math. Comput. Simulation, **80** (2010), 1082–1088.

[31] J. M. Hyde, M. K. Miller, M. G. Hetherington, A. Cerezo, G. D. W. Smith and C. M. Elliott, *Spinodal decomposition in Fe-Cr alloys: Experimental study at the atomic level and comparison with computer models—II. Development of domain size and composition amplitude*, Acta Metall. Mater., **43** (1995), 3403–3413.

[32] J. M. Hyde, M. K. Miller, M. G. Hetherington, A. Cerezo, G. D. W. Smith and C. M. Elliott, *Spinodal decomposition in Fe-Cr alloys: Experimental study at the atomic level and comparison with computer models—III. Development of morphology*, Acta Metall. Mater., **43** (1995), 3415–3426.

[33] T. Izumitani, M. Takenaka and T. Hashimoto, *Slow spinodal decomposition in binary liquid mixtures of polymers. III. Scaling analyses of later-stage unmixing*, J. Chem. Phys., **92** (1990), 3213–3221.

[34] T. Kaczynski, K. Mischaikow and M. Mrozek, "Computational Homology," **157** of Applied Mathematical Sciences, Springer-Verlag, New York, 2004.

[35] W. Kalies and P. Pilarczyk, *CHomP software*, Available from http://chomp.rutgers.edu.

[36] R. V. Kohn and F. Otto, *Upper bounds on coarsening rates*, Comm. Math. Phys., **229** (2002), 375–395.

[37] T. Y. Kong and A. Rosenfeld, *Digital topology: Introduction and survey*, Comput. Vision Graph. Image Process., **48** (1989), 357–393.

[38] P. Leßle, M. Dong and S. Schmauder, *Self-consistent matricity model to simulate the mechanical behaviour of interpenetrating microstructures*, Comput. Mater. Sci., **15** (1999), 455–465.

[39] P. Leßle, M. Dong, E. Soppa and S. Schmauder, *Simulation of interpenetrating microstructures by self consistent matricity models*, Scripta Mater., **38** (1998), 1327–1332.

[40] S. Maier-Paape and T. Wanner, *Spinodal decomposition for the Cahn–Hilliard equation in higher dimensions: Nonlinear dynamics*, Arch. Ration. Mech. Anal., **151** (2000), 187–219.

[41] A. Novick-Cohen, *Upper bounds for coarsening for the deep quench obstacle problem*, J. Stat. Phys., **141** (2010), 142–157.

[42] A. Novick-Cohen, "The Cahn–Hilliard Equation: From Backwards Diffusion to Surface Diffusion," Cambridge Univ. Press, Cambridge, 2013. (in preparation).

[43] A. Novick-Cohen and A. Shishkov, *Upper bounds for coarsening for the degenerate Cahn–Hilliard equation*, Discrete Contin. Dyn. Syst., **25** (2009), 251–272.

[44] Y. Oono and S. Puri, *Study of phase-separation dynamics by use of cell dynamical systems. I. Modeling*, Phys. Rev. A, **38** (1988), 434–453.

[45] R. L. Pego, *Front migration in the nonlinear Cahn–Hilliard equation*, Proc. Roy. Soc. London Ser. A, **422** (1989), 261–278.

[46] E. Sander and T. Wanner, *Unexpectedly linear behavior for the Cahn–Hilliard equation*, SIAM J. Appl. Math., **60** (2000), 2182–2202.

[47] A. Schmidt and K. G. Siebert, "Design of Adaptive Finite Element Software: The Finite Element Toolbox ALBERTA," **42** of Lecture Notes in Computational Science and Engineering, Springer-Verlag, Berlin, 2005.

[48] P. Sternberg, *The effect of a singular perturbation on nonconvex variational problems*, Arch. Rational Mech. Anal., **101** (1988), 209–260.

[49] T. Sullivan and P. Palffy-Muhoray, *The effects of pattern morphology on late time scaling in the Cahn–Hilliard model*, Abstract, American Physical Society, APS March Meeting, (2007).

[50] R. Toral, A. Chakrabarti and J. D. Gunton, *Large scale simulations of the two-dimensional Cahn–Hilliard model*, Physica A, **213** (1995), 41–49.

[51] T. Ujihara and K. Osamura, *Kinetic analysis of spinodal decomposition process in Fe-Cr alloys by small angle neutron scattering*, Acta Mater., **48** (2000), 1629–1637.

E-mail address: l.banas@hw.ac.uk

E-mail address: amync@tx.technion.ac.il

E-mail address: robert.nurnberg@imperial.ac.uk